Asian Power Electronics Journal

PERC, HK PolyU

Asian Power Electronics Journal, Vol. 12, No. 1, June 2018

First edition June 2018 Printed in Hong Kong by Reprographic Unit
The Hong Kong Polytechnic University

Published by

Power Electronics Research Centre
The Hong Kong Polytechnic University
Hung Hom, Kowloon, Hong Kong

ISSN 1995-1051

Editorial board

Honorary Editor

Prof. Fred C. Lee Electrical and Computer Engineering, Virginia Polytechnic Institute and State University

Editor

Prof. Yim-Shu Lee
Victor Electronics Ltd.

Associate Editors and Advisors

Prof. Philip T. Krien
Department of Electrical and Computer Engineering, University of Illinois

Prof. Keyue Smedley
Department of Electrcial and Computer Engineering, University of California

Prof. Muhammad H. Rashid
Department of Electrical and Computer Engineering, University of West Florida

Prof. Dehong Xu
College of Electrical Engineering, Zhejiang University

Prof. Hirofumi Akagi
Department of Electrical Engineering, Tokyo Institute of Technology

Prof. Xiao-zhong Liao
Department of Automatic Control, Beijing Institute of Technology

Prof. Hao Chen
Dept. of Automation, China University of Mining and Technology

Prof. Danny Sutanto
Integral Energy Power Quality and Reliability Centre, University of Wollongong

Prof. S.L. Ho
Department of Electrical Engineering, The Hong Kong Polytechnic University

Prof. Eric K.W. Cheng
Department of Electrical Engineering, The Hong Kong Polytechnic University

Dr. Norbert C. Cheung
Department of Electrical Engineering, The Hong Kong Polytechnic University

Dr. Edward W.C. Lo
Department of Electrical Engineering, The Hong Kong Polytechnic University

Dr. Martin H.L. Chow
Department of Electronic and Information Engineering, The Hong Kong Polytechnic University

Dr. Chi Kwan Lee
Department of Electrical and Electronic Engineering, The University of Hong Kong

Table of Content

Asian Power Electronics Journal, Vol. 12, No. 1, June 2018

An Investigation of Coils Used in Dynamic Wireless Charging for Electric Vehicles

Chen K. W. K[1]   Cheng K. W. E[2]

Abstract–The dynamic charging for electric vehicles (EVs), compared with stationary charging, has become an essential research direction for release users from long parking time. In this paper, the coupling theories of coils are analyzed in aspects of shapes, misalignment. The considerations of coils and ferrites when designing the dynamic wireless charging system for EVs are indicated by simulation results. A wireless charging platform based on inductive coupled power transmission is presented, and the analyses are proved in hardware. The power efficiency of the proposed system is up to 82.29% after improvement.

Keywords–Wireless power transfer, electric vehicles, coupling theory

I. INTRODUCTION

The wireless power transfer, also known as wireless charging in practice, has been a hot topic and gained much attention from governments, research groups and companies all over the world. The main process of this technology is to transfer energy from power source to electric load over an air gap. It is also developed in electric vehicle charging recently and wildly.

In the last 20 years this technology once again sparked the interest of researches around the world. At the University of Hong Kong, Dr. Ron Hui and his team performed research on planar low power inductive battery chargers based on a low power printed circuit board technology [1-2]. Almost at the same time, in Auckland New Zealand, Dr. Covic and Dr. Boys started looking into high power WPT applications for mostly static charging. They have published numerous patents and journal papers, in order to describe and to highlight multiple aspects of this technology, ranging anywhere from power electronics to various circuit topologies and coil designs and optimizations [3-7].

The dynamic charging, which allows the EV can get recharged without any parking time, gets its research popularity increasingly. The significant breakthrough in the development of this technology was made by many research groups and companies. One of them was the Korea Advanced Institute of Science and Technology (KAIST), who built a On-Line Electric Vehicle (OLEV) which can transfer 60 kW of power to the busses, and 20 kW to the SUV's with efficiencies of 70% and 83% respectively [8].

However, the power efficiency of wireless charging for EVs is still not satisfied if considering worldwide using. For better understanding the factors influencing the charging process, the coupling theory is introduced. The shapes of coils and ferrites and the misalignment between emitters and receivers are the key to study the coupling.

For coil design and its optimization, reference [9] proposed an asymmetric coil sets for EV, which achieved a stationary wireless charging system with 75% power efficient and large tolerance when the horizontal displacement happens. Although this paper gives an improved coil design, it not starts from the coupling theory. Reference [10] proposed a dynamic charging system, which consists of multi-output circuits and circular pads. It analyzes the model using coupling theory, but only the interval distance is set to be a variable when compares the situation.

In this paper, the coupling theory based on basic charging process is analyzed. The mathematic models are built and their simulation results are followed, considering the shapes of coils, vertical and lateral displacement, and aspect ratio. A charging system is proposed and the experiments are also proceeded to prove the analyses in hardware. The goal is to find the considerations of coil design that helps to improve lateral tolerance and save materials.

II. COUPLING THEORY OF COUPLED COILS

1. Circular Coils

1.1. Self Inductance

The placement of coupled circular coils is depicted in Fig. 1, where R_1 and R_2 is the radius of primary and secondary coils respectively, and the *t* is the lateral misalignment while h is the interval in vertical direction.

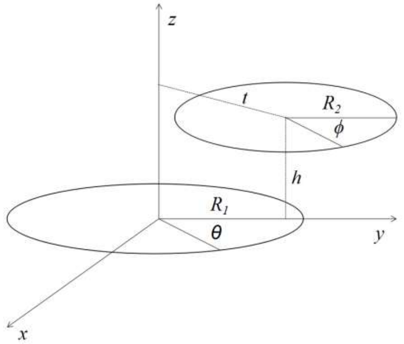

Fig. 1: Relative position of circular coils

As mentioned in the case study of inductance calculation [11], the self inductance is given by double integral Neuman formula as:

$$L_e = \frac{\mu}{4\pi}\oint_1\oint_2 \frac{d_{l_1} d_{l_2}}{r} = \frac{\mu}{4\pi}\int_0^{2\pi} d_\theta \int_0^{2\pi} \frac{R(R-r)\cos\varphi}{\sqrt{R^2+(R-r)^2-2R(R-r)\cos\varphi}} d_\varphi \tag{1}$$

Power Electronics Research Center, Department of Electrical Engineering, The Hong Kong Polytechnic University, Hong Kong
E-mail: [1]16091043g@connect.polyu.hk [2]eeecheng@polyu.edu.hk

where μ is the relative permeability of the medium.

In common cases, the radius of circle filament is much less than the curvature radius of coil, and the current is mainly distributed in the wire cross section [12]. Therefore, the internal self inductance when there is only one turn is given by:

$$L_i = \frac{\mu}{8\pi}(2\pi R) \tag{2}$$

1.2. Mutual Inductance

Based on the model shown above, we assume that R_1 and R_2 are the vectors of the primary and secondary circles. They are given by:

$$R_1 = R_1 \cos\theta \boldsymbol{x} + R_1 \sin\theta \boldsymbol{y} \tag{3}$$

$$R_2 = R_2 \cos(\theta+\varphi)x + \left[R_2 \sin(\theta+\varphi)+t\right]y + hz \tag{4}$$

$$|R_2\text{-}R_1| = \sqrt{\left[R_2\cos(\theta+\varphi)\text{-}R_1\cos\theta\right]^2 + \left[R_2\sin(\theta+\varphi)+t-R_1\sin\theta\right]^2 + h^2} \tag{5}$$

$$d_{l_1}\cdot d_{l_2} = R_1R_2\cos\theta d_\theta d_\phi \tag{6}$$

The case without lateral misalignment is simply given in [13] based on Neumann formula:

$$M = \frac{\mu}{4\pi}\int_0^{2\pi} d_\theta \int_0^{2\pi} \frac{R_1R_2\cos\varphi}{|R_2-R_1|} d_\varphi \tag{7}$$

Lateral and angular misalignment brings more complicated parameters considered in the computation process. An improved calculation method, which is named Magnetic Vector Potential Approach, is proposed in [14]. The situation of misalignment is considered. Based on [15], the equation for calculating the mutual inductance between filamentary coils with misalignment is given by：

$$M = \frac{2\mu}{\pi}\sqrt{R_1R_2}\int_0^{\pi} \frac{\left(\cos\theta - \frac{t}{R_2}\cos\phi\right)}{k\sqrt{V^3}} d_\phi \tag{8}$$

2. Rectangular Coils

2.1 Self Inductance

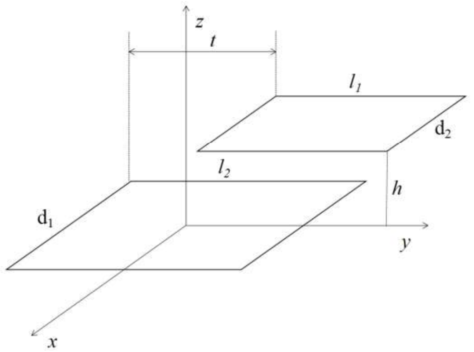

Fig. 2: Relative position of rectangular coils

To accurately compute the self-inductance of a rectangular coil, the magnetic field produced by a current element should be considered. Assuming that the current element has an unit length, the flux density generated by a straight line is given by Biot-Savart Law as:

$$B = \frac{\mu I}{4\pi\rho}\left[\frac{d-x}{\sqrt{\rho^2+(d-x)^2}} + \frac{d+x}{\sqrt{\rho^2+(d+x)^2}}\right] \tag{9}$$

The relative position of two coupled The relative position of two coupled rectangular coils has been illustrated in Fig. 2 , where l_1 and l_2 are the lengths of two coils, and d1 and d2 are their widths. And h is the vertical interval and t is the horizontal displacement, and r is the radius cross section of the winding wire. In this model, the turn of filament winding is assumed to be one for simple expression.

According to flux linkage method [16], the external self-inductance of rectangular coil can be expressed as:

$$\begin{aligned} L_e = \frac{\mu}{\pi}\Big[& 2\sqrt{(d_1-r)^2+(l_1-r)^2} - \sqrt{(d_1-r)^2+r^2} - \sqrt{(l_1-r)^2+r^2} + \sqrt{2}r + r\ln\left(\sqrt{2}-1\right)\Big] \\ & + (d_1-r)\left[\ln\left(\frac{\sqrt{(d_1-r)^2+(l_1-r)^2}-(d_1-r)}{l_1-r}\right) - \ln\left(\frac{\sqrt{r^2+(d_1-r)^2}-(d_1-r)}{r}\right)\right] \\ & + (l_1-r)\left[\ln\left(\frac{\sqrt{(l_1-r)^2+(d_1-r)^2}-(l_1-r)}{d_1-r}\right) - \ln\left(\frac{\sqrt{r^2+(l_1-r)^2}-(l_1-r)}{r}\right)\right] \\ & - r\left[\ln\left(\frac{\sqrt{r^2+(l_1-r)^2}-r}{l_1-r}\right) - \ln\left(\frac{\sqrt{r^2+(d_1-r)^2}-r}{d}\right)\right] \end{aligned} \tag{10}$$

Because the radius of wire is much smaller than the one of coil radius, so we have internal self-inductance as:

$$L_i = \frac{\mu}{8\pi}(2l_1 + 2d_1) \tag{11}$$

2.2 Mutual Inductance

The mutual inductance of coils with rectangular shape is simpler to be computed than coupled circular coils. The result could be the summation of the mutual inductance of four different edges. As illustrating in the rectangular coordinates, we could have the equation of elements in primary coil and secondary coil, which is given by:

$$d_{l_1} = a_1\boldsymbol{x} + b_1\boldsymbol{y} \text{ - } c_1\boldsymbol{x} \text{ - } d_1\boldsymbol{y} \tag{12}$$

$$d_{l_2} = a_2\boldsymbol{x} + b_2\boldsymbol{y} \text{ - } c_2\boldsymbol{x} \text{ - } d_2\boldsymbol{y} \tag{13}$$

According to Neumann formula, the mutual inductance between one of edges (a_1 and a_2) is given by:

$$M_{a_1a_2} = \frac{\mu}{4\pi}\oint\!\!\oint_{l_2 l_1} \frac{d_{l_1}d_{l_2}}{|\boldsymbol{r}_2-\boldsymbol{r}_1|} = \frac{\mu}{4\pi}\int_{-d}^{d}\int_{-e}^{e} \frac{d_{x_1}d_{x_2}}{\sqrt{(x_2-x_1)^2+h^2+(l_1-l_2+t)^2}} \tag{14}$$

Using the same equation, we could simply add the mutual inductance of other edges and get the total mutual inductance (the mutual inductance of two orthogonal edges is equal to zero):

$$M = M_{a_1a_2} + M_{b_1b_2} + M_{c_1c_2} + M_{d_1d_2} + M_{a_1c_2} + M_{a_2c_1} + M_{b_1d_2} + M_{b_2d_1} \tag{15}$$

III. COUPLING COEFFICIENT IN DIFFERENT SITUATIONS

1. Coupling Coefficient v.s. Vertical Misalignment When Different Coils are Used

In this part, the radius of circular coils, both primary and secondary coils, is set to be 20mm. Meanwhile, the width and length of every rectangular coil is 40mm in order to be the similar scale with circular ones. The lateral and horizontal displacements are ignored, and the vertical distance between primary and secondary coils is varied from 10mm to 40mm.

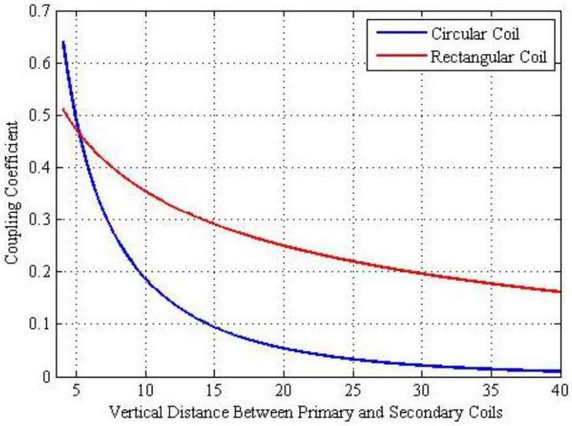

Fig. 3: Coupling coefficient v.s. vertical distance

The Fig. 3 shows the relationship between vertical distance h and coupling coefficient K. The blue and red lines are the result of circular coils and rectangular coils, respectively.
The circular coil has higher coupling coefficient when the vertical distance is lower than 5.3mm, approximately, but it will decrease rapidly after the distance become large. However, the rectangular coil will have much more slow reduction.

From the analysis, the reason why the circular coils are more widely adopted in litter air gap situation, such as cell phone charging, is obvious. But in the case of EV charging, the rectangular coils are more fit for air gap situation.

2. Coupling Coefficient v.s. Aspect Ratio
The aspect ratio can be expressed as followed:

$$m = l / d \qquad (16)$$

To be comparable, the width is constant at 40mm in calculation, while length varies from 1mm to 80mm. The air gap, which is known as h, is 15mm.

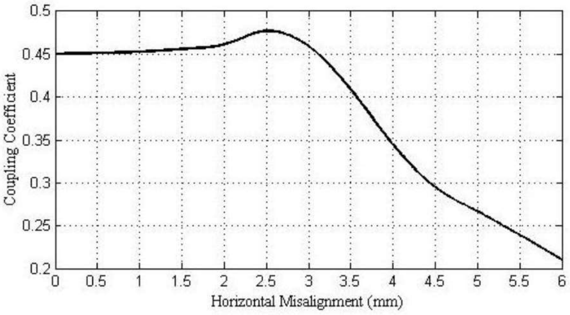

Fig. 5: Coupling coefficient v.s. horizontal displacement

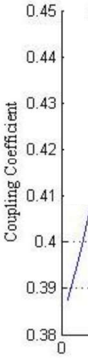

According to (14) and (15), the curve of coupling coefficient can be drafted and shown in Fig. 4. The coupling coefficient is small when the aspect ratio is small. When m is smaller than 0.25, the coupling coefficient increases rapidly with the rocket of length. But after the aspect ratio come to 0.5, the increasing trend of coupling coefficient becomes slow. When the length is 20mm and 40mm, the coupling coefficient is approx. 0.4342 and 0.4358, respectively.

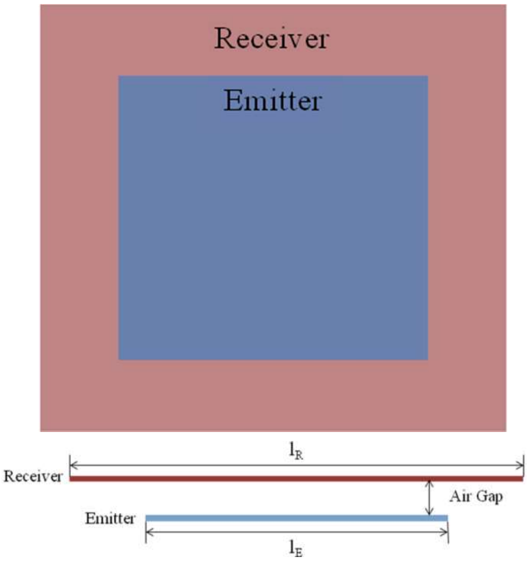

Fig. 6: Improved design of rectangular coils

Hence, for saving materials while maintaining the efficiency, the aspect ratio can be set as 0.5 when designing the coils.

3. Coupling Coefficient v.s. Horizontal Misalignment Based on Rectangular Coils

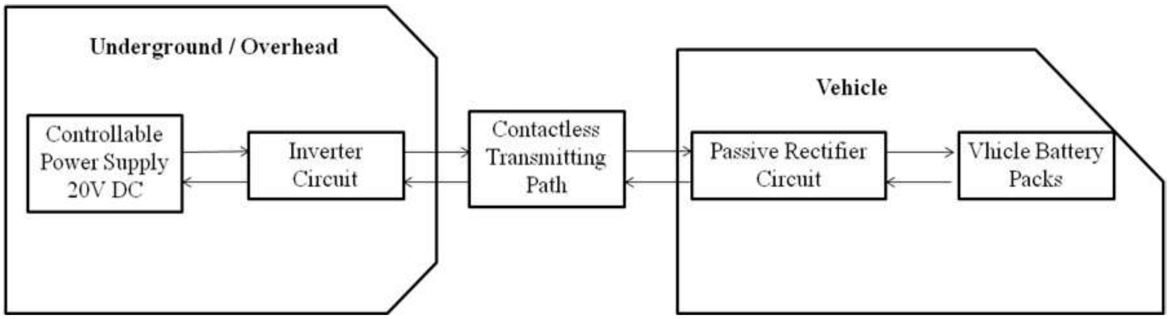

Fig. 7: Diagram of main charging circuit

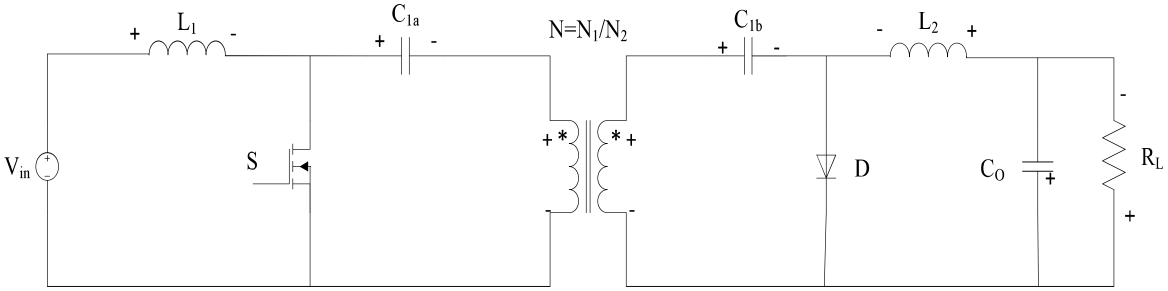

Fig. 8: Topology of main circuit

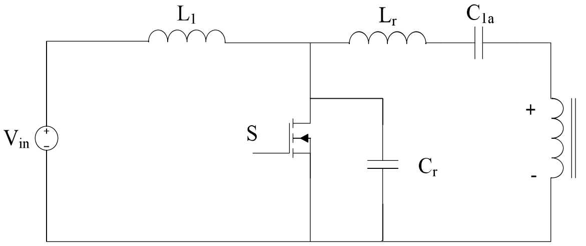

Fig. 9: Inverter with ZVS circuit

Similar to last part, the coupling coefficient is calculated when the horizontal misalignment happens when two coupled rectangular coils are used. The main parameters of coil size are also following the last section. The vertical distance h is 5mm. The horizontal displacement will vary from 0mm to 6mm in this research, while the length is set as 10mm. The result is depicted in Fig. 5.

There is a peak of coupling when the horizontal misalignment happens. After this peak, the coefficient will decrease rapidly. It indicates that when designing the system, the receiver coil should cover the emitter but in a suitable ratio, as the power transferred to second side is maximumed while the material is saved. The design consideration is illustrated in Fig. 6.

The l_m is the reluctant length of receiver, and l_m is equal to the half of the length of the emitter coil.

IV. WORKBENCH BUILDING

Fig. 7 shows the diagram of main charging circuit, the wireless charging path is the air gap which simulates the distance from vehicle chassis to the embedded emitter underground.

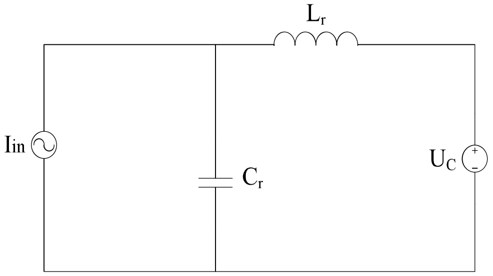

Fig. 10: ZVS Cuk Converter Equivalent Circuit

The topology of main circuit, including the inverter and rectifier, is shown in Fig. 8. To avoid the peak times of voltage over the switch and reduce swtiching loss, a simple Zero-Voltage-Switching circuit is implemented in the inverter, which can be seen in Fig. 9.

To design the resonant circuit, the equivalent circuit is drwan in Fig. 10. When the switch S is off and if L_1 has enough inductance, the power source and L_1 can be seen as a constant current source. Meanwhile, the diode in secondary side is working in freewheel operation, and the capacitor C_2 can be reflected into primary side. Thus, the From the equivalent circuit, the equations below can be extracted:

$$\begin{cases} I_{Cr} = C_r \dfrac{dU_{Cr}}{dt} \\ I_{Cr} = I_{in} + I_{Lr} \\ U_C - U_{Cr} = L_r \dfrac{di_{Lr}}{dt} \end{cases} \tag{17}$$

The initial conditions are as followed:

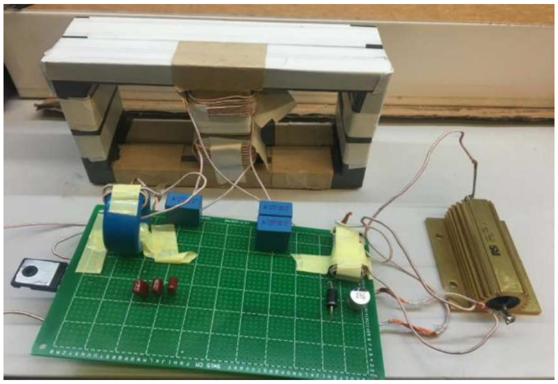

Fig. 11: Workbench of charging system

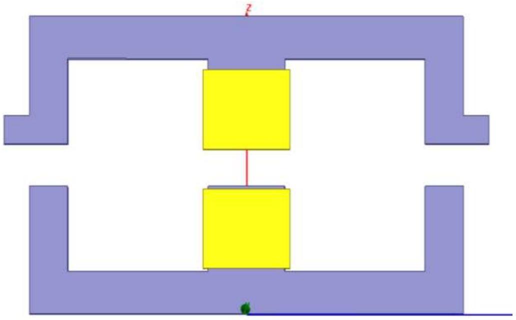

(a): No horizontal misalignment

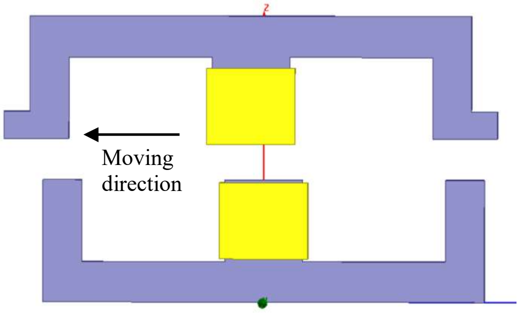

(b): Horizontal misalignment happens

Fig. 12: Experiment of horizontal misalignment

$$\begin{cases} U_{Cr}(0) = 0 \\ I_{Cr}(0) = I_{in} + I_{Lr0} \end{cases} \tag{18}$$

Where I_{Lr0} is the initial current of inductor.

I_{Lr0} can be decided by output current as:

$$I_{Lr0} = \frac{I_o}{n} \tag{19}$$

Based on the equations (17), (18) and (19), the voltage over resonant capacitor can be calculated:

$$U_{Cr} = \sqrt{U_C^2 + I_{Cr0}^2 \frac{L_r}{C_r}} \sin(\omega t - \theta) + U_C \tag{20}$$

Where the phase angle and angular speed are as followed:

Table 1: Parameters of Components

Component	Main Value
L_1	$50\mu H$
L_2	$10\mu H$
L_r	$10\mu H$
C_1	$1\mu F$
C_2	$2\mu F$
C_r	$1\mu F$
C_o	$100\mu F$
V_{in}	$20V$ DC

$$\begin{cases} \theta = \mathrm{arctg} \dfrac{U_C}{I_{Cr0}\sqrt{L_r/C_r}} \\ \omega = \sqrt{\dfrac{1}{L_r C_r}} \end{cases} \tag{21}$$

Starting from $t = 0$, the first time and second time when the U_{Cr} is crossing zero are:

$$\begin{cases} t_1 = (\pi + 2\theta)/\omega \\ t_2 = 2\pi/\omega \end{cases} \tag{22}$$

Between t_1 and t_2, the switch can achieve zero-voltage switching. From the analysis, it can be concluded that this circuit have a simple structure with easy control and less loss in components. If the inductance of transformer can be used as resonant inductor L_r, the additional components are only resonant capacitor. The resonant capacitor C_r is paralleled with switch S, absorbing the over-voltage and the high frequency ripple waves over the switch at the very time of turning off. Due to the time limitation allowing ZVS, this simple ZVS topology is suitable for stable loads situation, where the duty time of gate control signal is nearly constant.

The paremeters of all components are listed in Table 1. The ratio N is 1, and the voltage conversion of the converter is 1 consequently .

V. EXPERIMENTAL RESULTS

As for proving the simulation results, the experiments are proceeded in a low power workbench, with 80kHz frequency and 5mm air gap. The width and length of the center rectangular coils are both 30mm. The workbench is shown in Fig. 14. When there is no later misalignment and the load is a $9\,\Omega$ resistor, the input power is 48W, and the output power is 32.11W. The power efficiency is 66.89%. As the rectangular coil is more suitable for dynamic charging, the design consideration of it is more important. For improve the tolerance of later displacement, the design of the coil and its position is the very factors ferrites are used. Their placement is depicted in Fig. 12, where the lower one is the emitter and above it is receiver. The yellow part is the coils twined on the ferrites.

The results of experiments are presented in a oscilloscope, where the Channel 1 (yellow lines) is the output voltage, and Channel 2 (blue lines) represents the switching frequency and Channel 3 (purple lines) is the voltage over the switch S. From the results of scope, it is obvious that

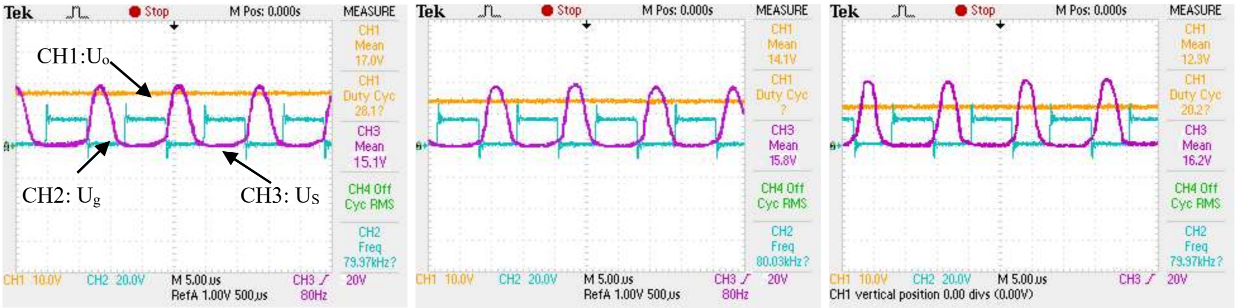

(a): Experiment result (Uo =17.0V) (b): Experiment result (Uo =14.1V) (c): Experiment result (Uo =12.3V)

Fig. 13: Output voltage of charging system (CH1: 2.5V/Unit, CH2: 4V/Unit, CH3: 4V/Unit)

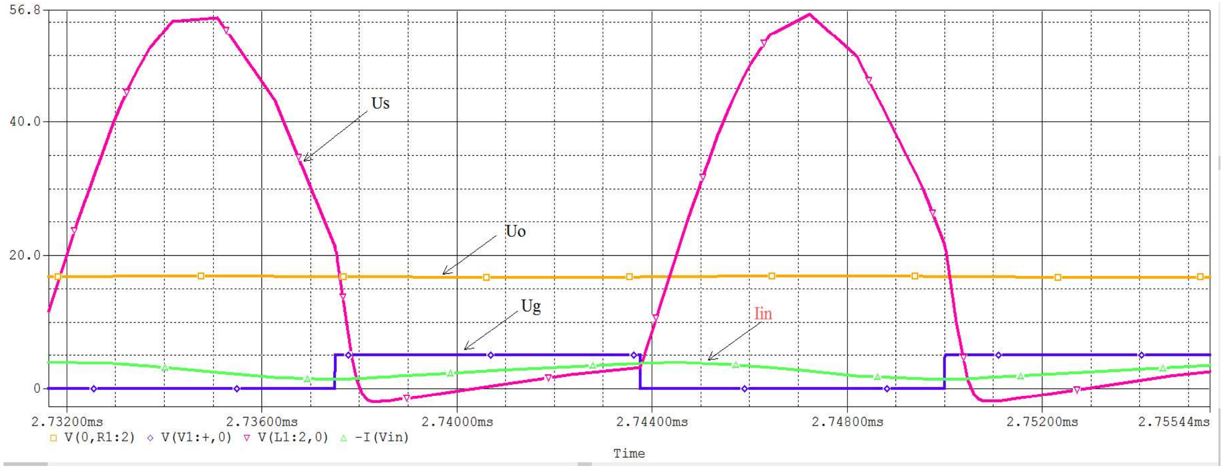

(a) R=9Ω

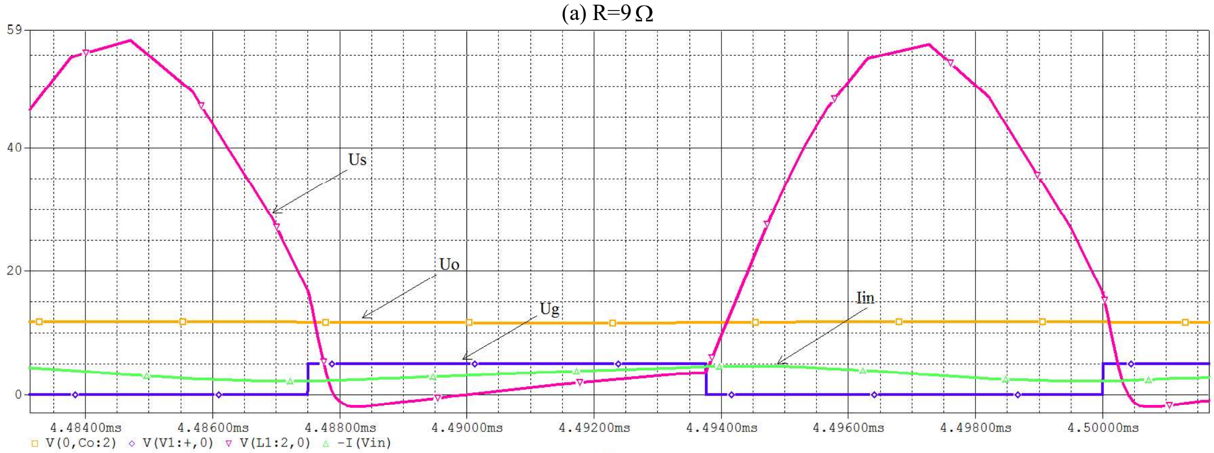

(b) R=2.5Ω

Fig. 15: System simulation results

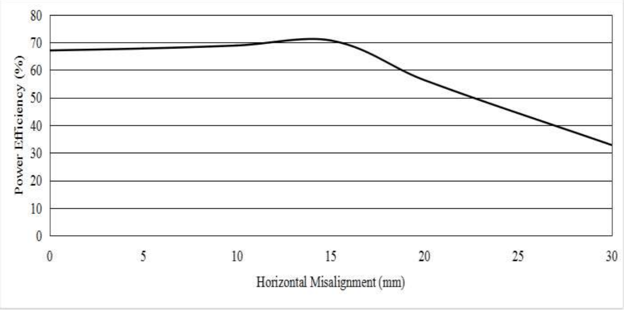

Fig. 14: Experiment results of power efficiency v.s. horizontal misalignment

the voltage over the switch will be reduced to zero just before it is turned on again. It proves that the ZVS is achieved and the resonant circuit is working effectively.

The outputs are sampled when the lateral movement distance is changing from 0mm to 30mm, and Fig. 13 shows three of the sampled results detected in the oscilloscope. The power efficiency curve which is changing with horizontal misalignment is shown in Fig. 14. From the results, it is obvious that the power efficiency has its peak when the horizontal misalignment is 15mm, which proves that the tolerance of the lateral displacement can be improved when the secondary coil covers the emitter coil.

The highest efficiency of the platform is 66.89%, which is not satisfied due to the non-matching load. Fig. 15 (a) and

(b) show the simulation results in PSPICE, when the load is 9Ω and 2.5Ω resistor respectively. When the 9Ω is as the matched loading and the coupling coefficient is 0.632, the output voltage is 17.3V which is also presented in experiment. The output voltage is 33.25W, and the power efficiency is 66.51%. After matching the load by using 2.5Ω resistor, the power efficiency is improved to 82.29% in the same coupling, where the output voltage is heightened to 57.6W.

VI. CONCLUSION

The coupling theory of EV dynamic wireless charging is discussed. The factors, shapes of coils, vertical and horizontal misalignment and aspect ratio are considered based on mathematic models. The simulation results are following the analyses. Based on the results, several conclusions of coil design are indicated as followed:

1. The rectangular coils are more suitable for EV dynamic charging.
2. The aspect ratio 0.5 (length/width) is helpful for saving materials while maintaining the power efficiency.
3. The receiver coils should cover the emitters with proper ratio (l_m = Emitter coils length/2).

The experiments are proceeded in a 80kHz low power workbench successfully. The ZVS resonant circuit is achieved successfully as to reduce the switch loss. The considerations introduced former are proved. The efficiency of the designed platform can be up to 82.29% after using well-matched load.

REFERENCE

[1] Tang, Sc, Ron Hui, Sy, and Chung, Hsh. "A Low-profile Power Converter Using Printed-circuit Board (PCB) Power Transformer with Ferrite Polymer Composite." 16, no. 4 (2001): 493-498.

[2] "Univ City Hong Kong Files European Patent Application for Planar Inductive Battery Charger." Global IP News. Electrical Patent News (New Delhi), January 16, 2014.

[3] Hao Hao, Covic, & Boys. (2014). "A Parallel Topology for Inductive Power Transfer Power Supplies." Power Electronics, IEEE Transactions on, 29(3), 1140-1151.

[4] Budhia, M., Boys, J.T., Covic, G.A., and Chang-Yu Huang. "Development of a Single-sided Flux Magnetic Coupler for Electric Vehicle IPT Charging Systems.(inductively Power Transfer)(Technical Report)." IEEE Transactions on Industrial Electronics 60, no. 1 (2013): 318.

[5] Keeling, N.A., G.A. Covic, and J.T. Boys. "A Unity-Power-Factor IPT Pickup for High-Power Applications." Industrial Electronics, IEEE Transactions on 57, no. 2 (2010): 744-751.

[6] Kissin, Michael L G, Grant A Covic, and John T Boys. "Steady-State Flat-Pickup Loading Effects in Polyphase Inductive Power Transfer Systems." Industrial Electronics, IEEE Transactions on 58, no. 6 (2011): 2274-2282.

[7] Huang, C.-Y., Boys, J. T., and Covic, G. A. "LCL Pickup Circulating Current Controller for Inductive Power Transfer Systems." IEEE Transactions on Power Electronics 28, no. 4 (2013): 2081-2093.

[8] Kong, Sunkyu, Bae, Bumhee, Jung, Daniel H., Kim, Jonghoon J., Kim, Sukjin, Song, Chiuk, Kim, Jonghoon, and Kim, Joungho. "An Investigation of Electromagnetic Radiated Emission and Interference From Multi-Coil Wireless Power Transfer Systems Using Resonant Magnetic Field Coupling." IEEE Transactions on Microwave Theory and Techniques 63, no. 3 (2015): 833-846.

[9] Choi Su Y., Jin Huh, Woo Y. Lee, and Chun T. Rim. “Asymmetric Coil Sets for Wireless Stationary EV Chargers with Large Lateral Tolerance by Dominant Field Analysis.” Power Electronics, IEEE Transactions on 29.12(2014): 6406-6420.

[10] Zhang X., Yuan Z. Y., Yang Q. X., Li Y. J., Zhu J. G., and Li Y. “Coil Design and Efficiency Analysis for Dynamic Wireless Charging System for Electric Vehicles.” Magnetics, IEEE Transactions on 52.7 (2016):1-4.

[11] Shatz Lisa F., and Christensen Craig W. "Numerical Inductance Calculations Based on First Principles." PLoS ONE 9, no. 11 (2014): PLoS ONE, Nov 17, 2014, Vol.9(11).

[12] Yao Luo and Baichao Chen. "Improvement of Self-Inductance Calculations for Circular Coils of Rectangular Cross Section." Magnetics, IEEE Transactions on 49, no. 3 (2013): 1249-1255.

[13] Babic S., C. Akyel and S.J. Salon. "New Procedures for Calculating the Mutual Inductance of the System: Filamentary Circular Coil-massive Circular Solenoid." Magnetics, IEEE Transactions on 39, no. 3 (2003): 1131-1134.

[14] Amos Anele O., Hamam Ykandar, Alayli Yasser, and Djouani Karim. "Computation of the Mutual Inductance between Circular Filaments with Coil Misalignment." AFRICON, 2013, 2013, 1-5.

[15] Anele, Hamam, Chassagne, Linares, Alayli, and Djouani. "Computation of the Mutual Inductance between Air-Cored Coils of Wireless Power Transformer." Journal of Physics: Conference Series 633, no. 1 (2015): 6.

[16] Snyder J. N. "Inductance Calculations Working Formulas and Tables (Book Review)." Mathematics of Computation 18, no. 85 (1964): 164.

Asian Power Electronics Journal, Vol. 12, No. 1, June 2018

New Magnetic Composite Based on Ni-Zn for Magnetic Screenings and Power Conversion with Its Recyclable and Formulable Features

Qi W. B   Cheng K. W. E

Abstract-The development of ferrites makes them can be widely used in the field of optics, electrics, sound, magnetism. Ni-Zn ferrite offer the possibilities of good magnetic properties and high electrical resistivity, together with large permeability at high frequency. However, the present Ni-Zn ferrite's properties are strongly influenced by the materials' composition and microstructure, which are sensitive to the preparation methodology used in their synthesis. Furthermore, it also need ferrite to answer strict environment and realize better properties with the recent trend. So, more improvement should be achieved. Here we proposed a modified way to prepare it, new polymer bonded Ni-Zn ferrite. We make effort to improve its magnetic property and formulate its tendency. We demonstrated to optimize the preparation technology including modifying the method of preparing magnetic powder and bonding with binder. Selection of materials is also important to its property. Through this work, new polymer bonded Ni-Zn ferrite presents high magnetic property and recyclable property. Further, through large amount of experiment data and basic knowledge, we can also formulate its magnetic property corresponding to its ratio.

Keywords-Polymer, ferrite, preparation, recyclable, formulate.

I. INTRODUCTION

Ni–Zn ferrites are soft ferrimagnetic materials having high resistivity values and low magnetic coercivity [1] and large permeability at high frequency [2]. Owing to good magnetic properties and high electrical resistivity, Ni-Zn ferrite could be an excellent material for power transformers in electronics, storage devices, microwave devices, magnetic fluids, and telecommunication applications, etc. [3–5].

However, the present ferrites are prepared by the conventional ceramic method, in which the stoichiometric composition and microstructure are extremely difficult to control. Additionally, the properties of Ni-Zn ferrite materials are strongly influenced by the materials' microstructure and composition, which are sensitive to the preparation methodology, such as the sintering conditions and the impurity levels present in or added to these materials could change their properties [6]. Therefore, the standardization and selection of an appropriate process is, the key to obtain good quality ferrites. The conventional method requires prolonged heating at high temperatures during preparation, which may cause some of the constituents to evaporate, thereby modifying the desired stoichiometry [7]. Moreover, in Ni–Zn ferrite, the volatilization of zinc at high temperatures results in the formation of Fe^{2+} ions, which increase electron hopping and reduce resistivity. The grinding or milling operations involved in the process lead to the loss of some material and to concentrations of impurities that result in non-stoichiometric compositions [8,9]. Consequently, samples always present unreproducible characteristics. So, we proposed a new way to bypass this problem.

Here we choose polymer bonded methods as a better alternative, since they overcome the instability of the conventional ceramic method, together with making the most of its advantage including efficiency and safety. The polymer bonded method has proved to be one of the effective routes because of its controllability and high efficiency. Including to decrease the cost and waste of preparation thus increase its efficiency. Varieties of bonded methods such as co-precipitation, hydrothermal synthesis, the citrate precursor method, the glass-ceramic route and the sol–gel process have been developed [10-12].

With the recent trend toward technology efficiency and excellence, polymer bonded ferrite must realize high magnetic property and mechanical property in an effective way. For this purpose, we make effort to optimize technology and materials, aim for getting high performance polymer bonded ferrite.

In this study, we prepared polymer-bonded ferrite through bonding magnetic powders and binder such as thermoplastic polymer at an appropriate mixing ratio with different methods by compression molding. The magnetic powder was usually obtained by gas atomization, melt quenching. Here we propose 2 methods to prepare magnetic powder through combustion reaction or the method that sintering and then smash it through atomization and ball milling. The combustion reaction synthesis method of magnetic powder preparation is a good choice, since they not only overcome the drawbacks of the conventional ceramic method, but also prepare nano-scale magnetic powders possess distinctive physical and chemical properties because of their nano-sized crystallite, large surface area and different surface properties (such as surface defect) etc. [13]. Then bonding magnetic powder and binder, mixture was then molded by machine. The advantage of this comprehensive method is that we can not only get good performance raw magnetic powder, but also can get the optimal powder size which is so important to the binding efficiency. Additionally, this method has the advantages of applying inexpensive raw materials and maintaining a relatively easy preparation process, moreover achieving a fine magnetic powder with high homogeneity. Hence, we can improve efficiency and magnetic performance through this new method.

Power Electronics Research Center, Department of Electrical Engineering, The Hong Kong Polytechnic University, Hong Kong
E-mail: webqi@polyu.edu.hk, eric-cheng.cheng@polyu.edu.hk

The method mixing magnetic powder and binder is also important to its property. The magnetic powder was first coupled with the acetone solution containing a silane coupling agent for improving bonding effect because magnetic powder is hydrophilicity and binder is hydrophobicity, through couple treatment, they can form strong chemical bonds. The schematics of coupling agent is shown in Fig. 1. Thus, it will increase the mechanical property of polymer bonded ferrite.

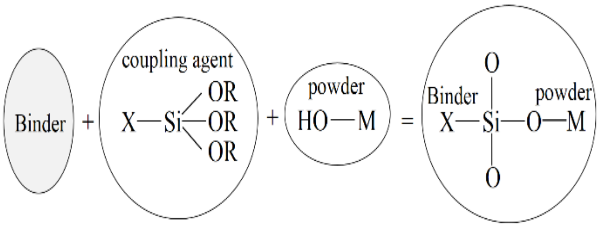

Fig. 1: Schematics of coupling agent.

In this study, we also optimize preparation process through improving the powder preparation and controlling its contents. We bypass the obstacle by calculating the magnetics parameters and clarify the relationship between the preparation conditions (magnetic powders and particle size of starting materials) and some properties of the bonded ferrite. We also design a recyclable polymer bonded ferrite through materials and process design under certain conditions.

II. EXPERIMENTAL PROCEDURE

The flow chart of the experimental procedure is shown in Fig. 2.

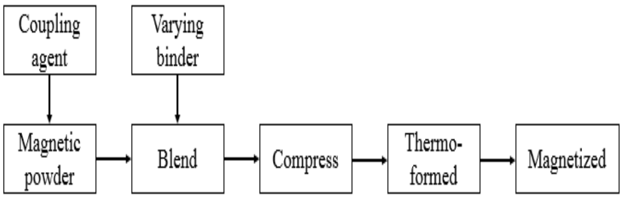

Fig. 2: Flow chart of experimental procedure in this study.

The samples were prepared by mixing magnetic powder and binder, and then combined through a compression-molding technique.

Here we propose 2 methods to prepare magnetic powder: sintering and combustion reaction.

The combustion reaction synthesis method, mix oxidizing reagents (such as nitrates) and reducing reagent (such as urea). And then the reaction happens spontaneously, this is because it is an exothermal reaction, thus, high temperatures generated will make oxides crystallize easily. Additionally, the reaction also prevents the instantaneous formation of particle agglomeration which will decrease product property dramatically [14]. The particle produced by this process have the advantage of chemical homogeneity on an atomic scale, uniform particle sizes and controlled particle shapes. Moreover, the reaction will not cause the loss of materials and impurity because there is no other media or steps. It can form magnetic powder directly [15-17]. This fact is important because contrast to the microstructures developed during indirect method (many steps to prepare magnetic powder), to a large extent, its powder's characteristics (crystallite size and shape, size distribution, porosity, state of agglomeration, chemical and phase composition) is more efficient and helpful to prepare magnets [18], which are closely associated with the processing method. Several investigations of the characteristics of Ni–Zn ferrites, such as their structure, electrical conductivity, chemical and elastic properties, dielectric behavior and magnetic properties, have been reported in the literature [19-21]. However, no study about polymer bonded magnets use Ni–Zn ferrite powders produced by this combustion reaction method. This study, investigated the character, the effect of the contents on the preparation efficiency and magnetic properties prepared by combustion reaction, then prepared with comprehensive method next step.

Combustion reaction method, showed in Fig. 3. Magnetic powder with a nominal composition of $Ni_{(1-x)}Zn_xFe_2O_4$, where x= 0.3, 0.4 and 0.5was prepared, including a heating reaction ($NiO+ZnO+Fe_2O_3=Ni_a Zn_{(1-a)} Fe_2O_4$) of a series mixture of metallic oxide (Ni, Zn and Fe), an exothermic reaction of a mixture of metallic nitrates (Ni, Zn and Fe) and urea (reducing agent). The materials used were zinc nitrate $Zn(NO_3)_2{\cdot}6H_2O$, nickel nitrate $Ni(NO_3)_2{\cdot}6H_2O$, iron nitrate $Fe(NO_3)_3{\cdot}9H_2O$ and urea (NH_2CONH_2). The proportions of the initial reagents were calculated based on the total valences of the reacting elements to maximize magnetic property and preparation efficiency, following the concepts of physics and chemistry [22-23]. Equation as follows:

$$(0.5-x)Ni(NO_3)_2\cdot 6H_2O+0.5-xZn(NO_3)_2\cdot 6H_2O+2Fe(NO_3)_3\cdot 9H_2O+8NaOH=Ni_{(0.5-x)}Zn_{(0.5-x)}Fe_2O_4+8NaNO_3+28H_2O.$$ [24]

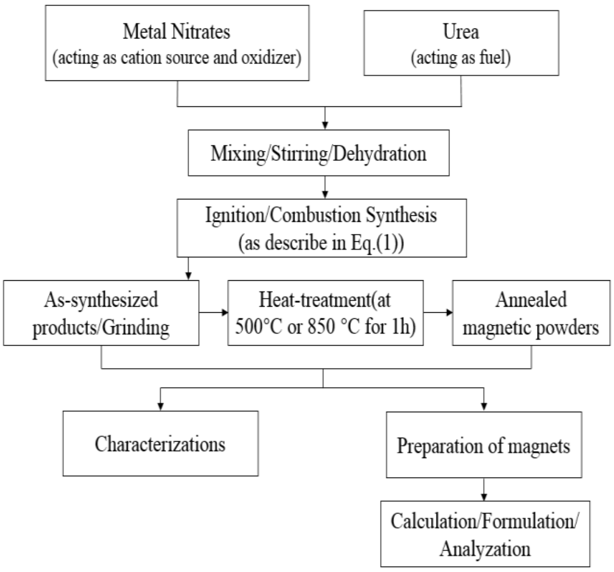

Fig. 3: Flow chart of combustion reaction method in this study

Sintering method, powder Fe_2O_3, NiO, CuO, ZnO were chosen as the raw materials to prepare NiZn ferrites. The molar percentage of the raw materials is listed in Table 1. First, all oxides were mixed with alcohol in a ball mill, according to their molar ratios. The mixture was then milled to 0.8 mm average particle sizes, respectively. Then the slurry was dried at 70°C. Second, pre-sintering them in muffle furnace at 950°C for 3h. The calcinations were then conducted in air for 3h. Third, the calcined powders were mixed with distilled water and 0.2mol% V_2O_5 then ground in a centrifugal ball mill until the powders reached an average particle size of 0.8 mm. The powders were then dried at 70°C. Fourth, calcine them in muffle furnace at 1150°C for 3h. The calcinations were then conducted in air for 3h. Finally, ball mill them into appropriate particle size for next step.

Table 1: Chemical compositions of samples

Sample no.	Fe_2O_3 (mol%)	ZnO (mol%)	NiO (mol%)	CuO (mol%)
1	50	30	20	0
2	50	30	17.5	2.5
3	50	30	15	5

The magnetic powder was then coupled with the acetone solution containing a silane coupling agent and was dried in an oven. The coupled magnetic powder was mixed uniformly with varying binder proportions of PMMA and curing agent [25]. The resulting mixtures were compressed to E-core samples at different pressure levels. Then thermoformed for two hours at different thermosetting temperatures. The samples were then magnetized using a high pulse magnetic field magnetizer at a voltage of 1400 V, which was sufficient to generate 4500 Oersted field strength to saturate the bonded Ni-Zn ferrites. The magnetic properties were measured by a HIOKI3532-50 LCR HiTESTER. All tests were carried out at room temperature.

III. RESULTS AND DISCUSSION

III.I. Magnetic properties

A series of preparation process were needed to prepare our sample in different conditions to determine the magnetic property and mechnical property. We label method 1 as preparing magnetic powders by combustion reaction and then bonded with epoxy resin, method 2 as preparing magnetic powders by sinstering method and then bonded with epoxy resin.

Fig. 4 shows the morphology of magnetic powders produced by 2 methods. From this picture, we can analyze powder's characteristics (powder size, degree of purity) visually. It shows that the powders prepared by method 1 , its powders size is smaller and powder is more pure compared with powder prepared by method 2. The light spot shows impurities exist in powders prepared by sinstering ways, it is because when ball milling it, some impurities doped.

Fig. 4: Morphology of magnetic powders prepared by 2 methods. method1(on the right), method2(on the left)

Fig. 5 presents the morphology of polymer bonded ferrite with different preparation, we can see that E-core prepared by method 1(on the right) is more uniform. Additionally, when we test their mechanical property, sample prepared by method 2 is more brittle and easily destroyed once we exert big force. Its mechanical property is worse compared with samples prepared by method 1.

Fig. 5: Morphology of E-core prepared by 2 methods method1(on the right), method2(on the left)

From this we can see that powder property prepared by method 1 is superior to method 2 whether in powder size or uniformity. Additionally, mechnical property is also corresponding to powder property.

III.II. Magnetic properties

Magnetic property determines whether polymer bonded ferrite can be commercially used or not. To get high-performance ferrite, we try to clarify the correlation between the material constants and μ_r in the polymer bonded ferrite which will help us optimize technology and formulate results.

The result μ were measured by a HIOKI3532-50 LCR HiTESTER. All test results below were calculated at the frequency of 50KHz.

The ratio of binder is an important factor that influences magnetic properties. Table 1 presents the magnetic properties of 1.5wt% - 6.0wt% binder ratio bonded magnets with same preparation technology. All experiment results have set standards and control variables, such as all materials should be the same, and prepared in 1 batch. Then calculate magnetic properties according to the following formulas:

$$\mu_e = \frac{L\, L_e}{0.4\pi N^2 A_e}$$

where L is sampler's length(cm); Le is the Inductance(μH), it is measured by HIOKI3532-50 LCR HiTESTER; N is the numbers of turns; A_e is effective sectional area(cm^2).

From this table, we can see that μ of the bonded ferrite decreased with the increasing of the ratio, while mechanical property increased when binder content increased. Moreover, when the ratio is less than 5%, the μ decreases slower than the ratio is bigger than 5%.

Table 1: Magnetic properties of magnets containing 1.5 wt% - 6.0 wt% binder content at 620 MPa pressure

Binder content	μ_e
1.5 wt.%	107.9
2.0 wt.%	104.4
2.5 wt.%	102.7
3.0 wt.%	100.0
3.5 wt.%	99.3
4.0 wt.%	96.8
4.5 wt.%	93.4
5.0 wt.%	92.5
5.5 wt.%	83.5
6.0 wt.%	80.2

Fig. 6 presents the tendency chart of different bonded ferrite with corresponding ratio, we can see variation tendency is not sharp, thus we can formulate tendency of μ through formula on the base of physics.

$$\mu = -0.05x^3 + 0.7x^2 - 4.7x + 111.8$$

x is the ratio of binder.

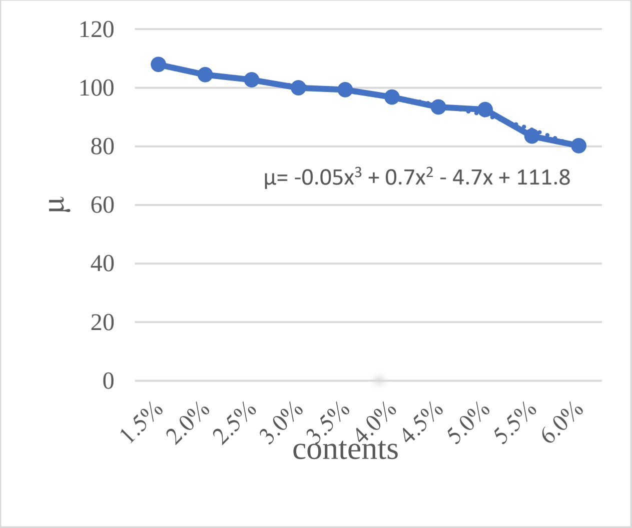

Fig. 6: Magnetic property of different ratio bonded ferrite.

The preparation method greatly determines its magnetic property. To get effective magnetic powders, we use 2 methods to prepare which were mentioned above, then addressed them with varying parameters.

Fig.7 presents the μ of samples with different parameters. It shows that the role of compacting pressure and binder's ratio is too small compared with catagolories of magnetic powder in influence magnetic property. The caculated μ prepared by method 1 is average 100, and few change whatever ratio and pressure changed. The same results can be indicated in method 2. It shows that category of magnetic powder is determining factor that influence magnetic property of bonded ferrite. Moreover, magnetic powder is determined by its preparation method. Method 1 is superior than method 2.

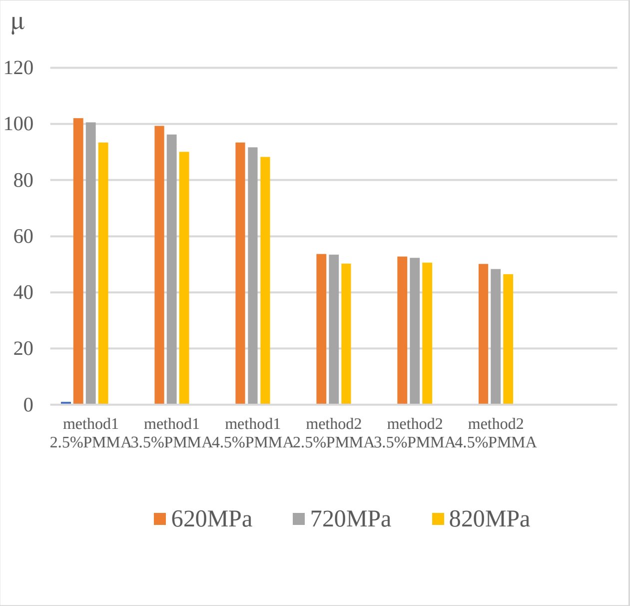

Fig. 7: Magnetic property prepared by 2 methods.

Different frequency may affect the u$_r$, it will influence application. So, we measured samples in different frequency, results showed in Fig.8. We can see in high frequency 50KHz or 100KHz, the μ are almost the same with each other, its magnetic property is so stable in high frequency.

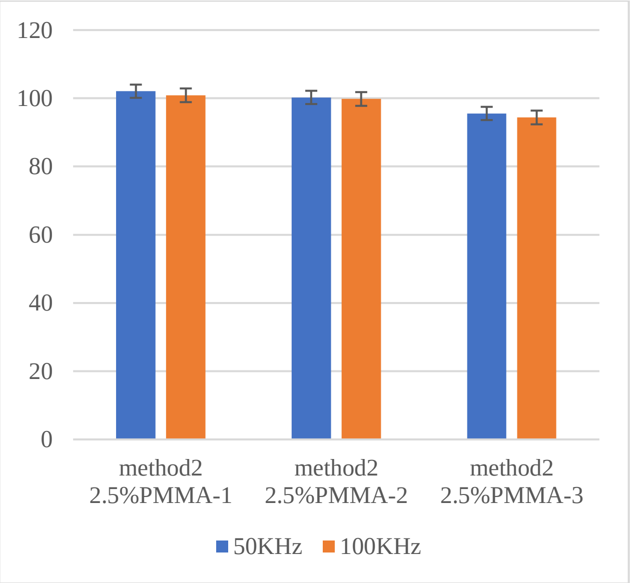

Fig. 8: Magnetic property measured in different frequency

III.III. Recyclable

Because when we prepare polymer bonded ferrite, some needed binder can be highly dissolved in aceton solution. So we try to design a new kind of ferrite in the investigation which was to develop recyclable polymer bonded ferrite with good performance at the same time. We designed a soluable binder which contain resin and curing agent, owing to they can not only thermoformed, but also dissolve to acetone under certain conditions. That means we can reuse it as a possible material for next time.

Fig. 9 presents the changes of recyclable ferrite after adding various amounts of acetone on the surface. The left one is that adding some drops of acetone, then press it. From the picture, we can see that dissolved area only exist in the areas where add acetone. The right one is that adding more acetone, then press it. We can see that the most of sample was dissolved. Thus, the recyclable polymer bonded ferrite can be dissolved in corresponding acetone. Such recyclable feature could be appealing in applications because it can save materials.

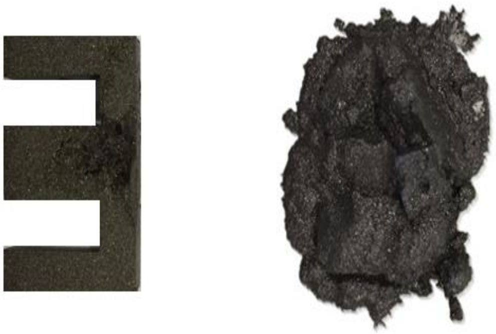

Fig. 9: changes of recyclable ferrite after a period of time

IV. CONCLUSIONS

The polymer bonded ferrites is efficiency and recyclable owing to the flexibility of materials and preparation technology. Further,we formulate the μ with different ratio based on physics.

We have developed a new polymer bonded ferrites using novel preparation technology with a series way of preparing magnetic powder, blending, and thermoformed. Different prepartion and different materials can infuence the magnetic property, meanwhile, compared with ratio and molding conditions, prepation of magnetic powder play a more improtant role. The magnetic powder prepared by combustion method is superior to the powder prepared by sinstering method whether in mechanical or magnetic property. We also note that the μ/ratio can be calculated on the basis of the measured, and physics. The magnetic property is also stable in high frequency. Such polymer bonded ferrites have the potential to be cost effective and recyclable, and to have applicable magnetic property.

V. ACKNOWLEDGE

The author gratefully acknowledged the support of Research Office, The Hong Kong Polytechnic University under project number H-ZDAT.

REFERENCES

[1] Kumar P S A, Shrotri J J, Kulkarni S D, et al. Low temperature synthesis of Ni 0.8 Zn 0.2 Fe 2 O 4, powder and its characterization. Materials Letters, 1996, 27(6):293-296.

[2] Tsay C Y, Liu K S, Lin T F, et al. Microwave sintering of NiCuZn ferrites and multilayer chip inductors. Journal of Magnetism & Magnetic Materials, 2000, 209(1–3):189-192.

[3] Bhise B V, Dongare M B, Patil S A, et al. X-ray infrared and magnetization studies on Mn substituted Ni-Zn ferrites. Journal of Materials Science Letters, 1991, 10(15):922-924.

[4] Slick P I. Ferrites for Non-Microwave Applications. Handbook of Ferromagnetic Materials, 1980, 2:189-241.

[5] Abraham T. Economics of ceramic magnets. American Ceramic Society Bulletin, 1994, 73(8):62-65.

[6] Rao B P, Rao P S V S, Rao K H. X-ray and magnetic studies of scandium substituted Ni-Zn ferrites. IEEE Transactions on Magnetics, 1997, 33(6):4454-4458.

[7] Zhang X H, Xiong W H, Li Y F, et al. Effect of process on the magnetic and mechanical properties of Nd–Fe–B bonded magnets[J]. Materials & Design, 2009, 30(4):1386-1390.

[8] Verma A, Goel T C, Mendiratta R G, et al. High-resistivity nickel–zinc ferrites by the citrate precursor method. Journal of Magnetism & Magnetic Materials, 1999, 192(2):271-276.

[9] Verma A, Goel T C, Mendiratta R G. Frequency variation of initial permeability of NiZn ferrites prepared by the citrate precursor method[J]. Journal of Magnetism & Magnetic Materials, 2000, 210(1–3):274-278.

[10] Kumar P S A, Shrotri J J, Deshpande C E, et al. Systematic study of magnetic parameters of Ni–Zn ferrite synthesized by soft chemical approaches. Journal of Applied Physics, 1997, 81(8):4788-4790.

[11] Albuquerque A S, Ardisson J D, Macedo W A A. A study of nanocrystalline NiZn-ferrite–SiO 2, synthesized by sol–gel. Journal of Magnetism & Magnetic Materials, 1999, 192(2):277-280.

[12] Dias A, Moreira R L. Chemical, mechanical and dielectric properties after sintering of hydrothermal nickel–zinc ferrites. Materials Letters, 1999, 39(1):69-76.

[13] Lin W H, Jean S K J, Hwang C S. Phase formation and composition of Mn–Zn ferrite powders prepared by hydrothermal method. Journal of Materials Research, 1999, 14(1):204-208.

[14] Shobana M K, Rajendran V, Jeyasubramanian K, et al. Preparation and characterisation of NiCo ferrite nanoparticles. Materials Letters, 2007, 61(13):2616-2619.

[15] Neto E F. Synthesis of silicon nitride by conventional and microwave carbothermal reduction and nitridation of rice hulls. Advanced Powder Technology, 2014, 25(2):654-658.

[16] Sousa V C, Segadães A M, Morelli M R, et al. Combustion synthesized ZnO powders for varistor ceramics. International Journal of Inorganic Materials, 1999, 1(3–4):235-241.

[17] Huang J, Su P, Wu W, et al. Preparation of Magnetic Cu 0.5 Mg 0.5 Fe 2 O 4, Nanoparticles and Kinetics of Thermal Process of Precursor. Journal of Superconductivity & Novel Magnetism, 2012, 25(6):1971-1977.

[18] Ibetombi Soibam, Sumitra Phanjoubam, Chandra Prakash, et al., “Structural, electrical and magnetic studies of Li–Zn–Ni Ferrites”, Modern Physics Letters B, 2010, 24(21):2277-2282.

[19] Verma A, Goel T C, Mendiratta R G, et al. Dielectric Properties of NiZn Ferrites Prepared by the Citrate Precursor Method. Materials Science & Engineering B, 1999, 60(2):156-162.

[20] Verma A, Goel T C, Mendiratta R G, et al. High-resistivity nickel–zinc ferrites by the citrate precursor method. Journal of Magnetism & Magnetic Materials, 1999, 192(2):271-276.

[21] Reddy M P, Madhuri W, Reddy N R, et al. Magnetic properties of Ni-Zn ferrites prepared by microwave sintering method. Journal of Electroceramics, 2012, 28(1):1-9.

[22] Jain S R, Adiga K C, Verneker V R P. Thermochemistry

and lower combustion limit of ammonium perchlorate in presence of methylammonium perchlorates. Combustion & Flame, 1981, 40(2):113-120.

[23] Peng C H, Hwang C C, Wan J, et al. Microwave-absorbing characteristics for the composites of thermal-plastic polyurethane (TPU)-bonded NiZn-ferrites prepared by combustion synthesis method. Materials Science & Engineering B, 2005, 117(1):27-36.

[24] Costa A C F M, Tortella E, Morelli M R, et al. Synthesis, microstructure and magnetic properties of Ni–Zn ferrites. Journal of Magnetism & Magnetic Materials, 2003, 256(1):174-182.

[25] Xiao J, Otaigbe JU, Jiles DC. Modeling of magnetic properties of polymer bonded Nd–Fe–B magnets with surface modifications. J Magn Magn Mater 2000;218:60–6.

Asian Power Electronics Journal, Vol. 12, No. 1, June 2018

Comparison Study of Rare-earth-free Motors with Permanent Magnet Motors in EV Applications

Zhu J. W. Cheng K. W. E. Xue X. D.

Abstract-Four topologies of in-wheel motors, including three switched reluctance motors and one permanent magnet synchronous motor of the same dimension, are proposed for comparison in electric vehicle applications. The three switched reluctance motors are 6/4, 6/10 and 6/16 two-teeth structures, respectively, along with the permanent magnet synchronous motor topology of 12 stator slot and 8 poles. The parameters of the motors are optimized for the best torque performance through genetic algorithm. The comparison contains torque output, iron loss and efficiency. Consequently, the results demonstrate 6/16 two-teeth switched reluctance topology is a potential candidate for electric vehicle applications.

Keywords-Finite element analysis, torque, iron loss, efficiency

I. INTRODUCTION

Owing to its efficient utilization of energy and ability to relieve environmental pollution in urban areas, the electric vehicle (EV) is receiving more and more attention. As a major power supply for vehicle operation, electric machines own the dominant advantage of much higher efficiency compared with the internal combustion engine (ICE), which may own even less than 20% efficiency for vehicle application. Therefore, the design of electric machines for EV application is quite a hot topic nowadays.

Electric machines can be divided into two categories: permanent magnet (PM) machines and rare-earth free machines. The PM motor owns a dominant position in EV applications due to its features of higher torque density and lower volume. It can also be classified into two groups on the basis of PM position: permanent magnet sychronous motor (PMSM) with PM on the rotor and flux switching motor (FSM) with PM inserted into the stator. Both of them have been applied widespread to EVs.

A thermal model of a water-cooled PMSM for EV propulsion is proposed to avoid demagnetization of PM material [1]. Design strategies of variable flux permanent magnet synchronous machine (VF-PMSM) are put forward to meet the requirement of reduced loss [2]. A vector flux-weakening control method is developed to extend motor speed range for EV drive system [3]. A new sound quality evaluation method of noise of PMSM is proposed in [4]. A novel calculation method on current charateristics of a vector inverter is proposed [5].

A Partitioned-Stator FSM with mechanical parts is proposed for EVs [6]. A high torque density and efficiency FSM with robust rotor structure is analyzed for high power applications [7]. A novel FSM with PM inserted in the rotor is developed in [8]. Kim [9] proposes a novel axial FSM to eliminate even harmonics for EV applications.

For the application of rare-earth free motors to EVs, the switched reluctance motor (SRM) occupies the major part due to its features of simple and robust configuration, fault tolerant capability and wide speed range. Design and analysis of a high-torque-density rotor segmented SRM is proposed for direct drive application [10-11]. A high efficiency and torque density SRM is developed for vehicle propulsion [12]. Chiba proposes a high torque density of 45Nm/L SRM for hybrid vehicles [13].

For EV applications, FSM is not as competitive as PMSM for in-wheel applications as a result of high magnetic saturation in the stator caused by coexistence of armature windings and PM material [7], limited area for copper windings [14]. Therefore, in this paper, PMSM and SRM are selected as comparison candidates. The SRMs contain a conventional 6/4 SRM, a 6/10 SRM with more rotor poles than stator poles [15] and a 6/16 SRM combining more rotor poles than stator teeth and multiple teeth per stator pole together [16], while the PMSM is a surface-mounted type. All of the four topologies are in-wheel version for comparison. Section II illustrates the characteristics of the motor topologies and their design considerations. Section III put forward the performance comparison of the four motors, including torque output, iron loss and efficiency. Section IV concludes the whole paper.

II. CHARACTERISTICS ANALYSIS & DESIGN CONSIDERATIONS FOR THE FOUR MOTORS

From theoretical analysis, the torque formula of the PMSM can be expressed as follows:

$$T_e = \frac{3}{2} p[\frac{(L_q - L_d)}{2} I_m^2 \sin 2\varphi_i + I_m \psi_m \cos \varphi_i] \quad (1)$$

where p is the pole pair number, I_m is the peak value of sinusoidal current, ψ_m is the PM excited flux linkage, φ_i is the internal power factor angle, L_q and L_d is the inductance of q axis and d axis, respectively. For surface-mounted PMSM, L_q is equal to L_d, so the torque equation can be simplified as,

$$T_e = \frac{3}{2} p I_m \psi_m \cos \varphi_i \quad (2)$$

For the SRM, the torque formula can be obtained from,

Power Electronics Research Center, Department of Electrical Engineering, The Hong Kong Polytechnic University, Hong Kong
E-mail: jingwei.zhu@connect.polyu.hk

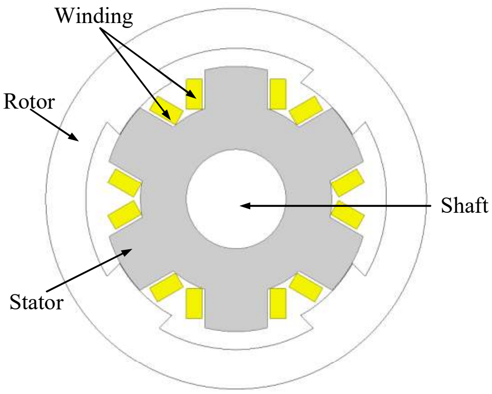

Fig. 1: (a) 6/4 SRM

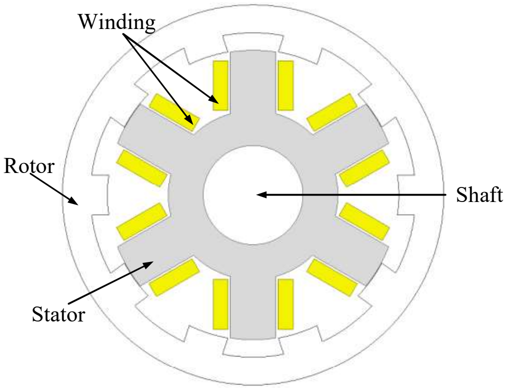

Fig. 1: (b) 6/10 SRM

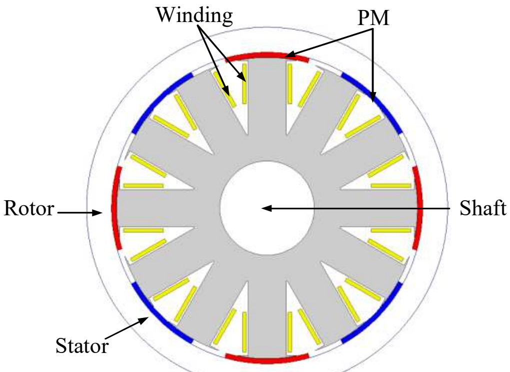

Fig. 1: (c) 12-stator-slot 8-pole PMSM

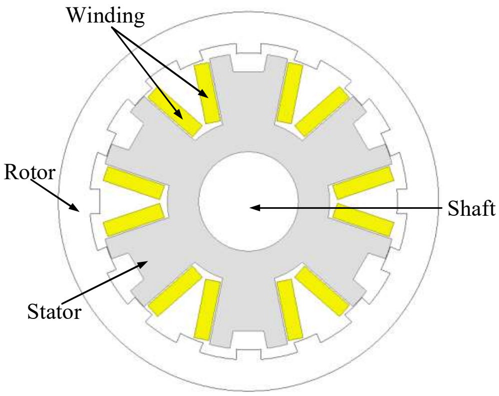

Fig. 1: (d) 6/16 two-teeth SRM

$$T_e = \frac{\partial W_m}{\partial \theta} \tag{3}$$

where W_m is the field co-energy and θ is the rotor position. The torque can be calculated further as [16],

$$T_e = \int \frac{N^2 I \mu_0 m l r}{2 l_g} di \tag{4}$$

where m is the number of teeth per pole, r is the outer radius of the stator, l_g and l is the airgap and stack length, respectively; μ_0 is magnetic permeability in the vacuum and N is number of turns per phase.

For in-wheel applications, the overall dimension of the motors should be determined initially. Because of the inner stator and outer rotor structure, the outer rotor diameter is selected as 382 mm, same as that in [17]. Due to the limitation of the wheel width, the stack length is set as 74 mm and the airgap length is chosen as 0.5 mm. The SRMs are 6/4, 6/10 and 6/16 topology, separately, while the PMSM is 12 stator slot and 8 PM poles.

For the optimization process, genetic algorithm (GA) method is utilized for multi-variable optimization. The objective function is the torque output. As a consequence of air cooling condition for in-wheel applications, the current density is limited to 5A/mm^2. Because of concentrated winding topology, the slot packing factor is selected as 0.44. By setting a suitable population number, maximum generation, crossover probability, elite count and mutation ratio, and utilizing rank fitness scaling, stochastic uniform selection, the final optimized four motor topologies are shown in Fig. 1. Besides, their parameters can be obtained from Table I.

Table I
Basic Parameters of the Four Motors

Dimensions	6/4 SRM	6/10 SRM	12/8 PMSM	6/16 SRM
Rotor outer diameter D_{r2} (mm)	382	382	382	382
Stator outer diameter D_{s2} (mm)	274	291	318	298
Stack length l (mm)	74	74	74	74
Airgap length l_g (mm)	0.5	0.5	0.5	0.5
Stator pole/teeth arc angle θ_s (degree)	27	18	22.5	8
Rotor pole arc angle θ_r (degree)	32	16	-	9.5
Number of turns per phase N	132	248	192	204
PM thickness (mm)	-	-	5	-
PM arc angle (degree)	-	-	31.5	-
Steel type	DR510	DR510	DR510	DR510
Copper wire diameter (mm)	1.12	1.12	1.12	1.12
Number of parallel windings	8	8	8	8
Slot fill factor	0.44	0.44	0.44	0.44

III. PERFORMANCE ANALYSIS & COMPARISON

The performance of the four topologies is calculated and analyzed by using finite element method (FEM), including torque characteristics, energy loss, power output and efficiency.

A. Comparison of three SRMs

For conventional SRMs, the torque density is relatively lower due to the elimination of PM materials. The 6/10 SRM is able to enlarge the slot area for more copper windings by increasing the number of rotor poles in order to provide enough torque output. The 6/16 two-teeth topology owns the capability to enhance torque output by enabling magnetic flux to pass through two divided teeth and enlarging the area for windings as illustrated in equation (4). The curves of the flux linkage of the three SRMs based on FEM at the unaligned and aligned position can be acquired from Fig. 2. Besides, the torque curve of one-phase conducting with the rated current during half an electric period can be obtained from Fig. 3 with the unaligned position set as zero degree.

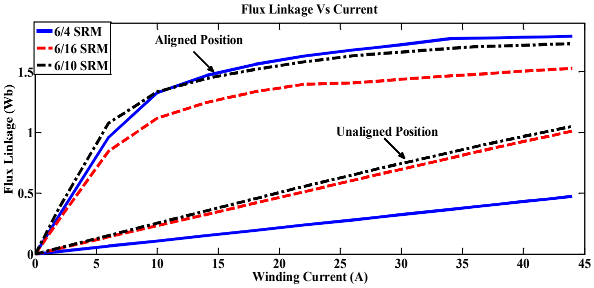

Fig. 2: Flux linkage of the three SRMs

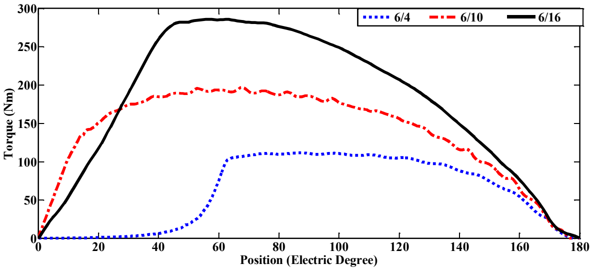

Fig. 3: Torque curves of SRMs for half an electric period conducting

Although the difference between the aligned and unaligned position for 6/10 and 6/16 SRM topologies is smaller than that of 6/4 SRM, the number of striking times for 6/10 SRM is 2.5 times as many as that for 6/4 SRM and the multiple teeth topology of 6/16 SRM doubles the striking times, along with increasing the striking times by more rotor poles. The torque improvement of 6/10 and 6/16 SRMs is demonstrated in Fig. 3 indicating the advancement of the topologies.

B. Comparison of PMSM with SRMs

The comparison is on the basis of in-wheel motors for EV applications. The current density is limited to 5A/mm^2 because of air cooling condition and the rated speed is 1000 rpm. The magnetic flux densities of the four motors at rated power are shown as below in Fig. 4.

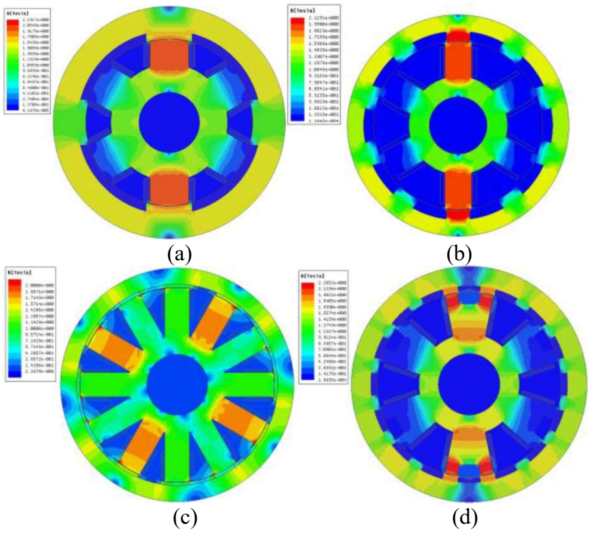

(a) (b)

(c) (d)

Fig. 4: Magnetic flux density of (a) 6/4 SRM (b) 6/10 SRM (c) 12/8 PMSM (d) 6/16 two-teeth SRM

The torque performance of the above four topologies at the rated speed with full phase conducting can be obtained from Fig. 5 by using FEM.

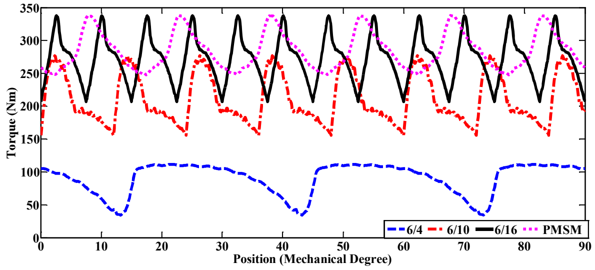

Fig. 5: Torque characteristics comparison of the four topologies

Fig. 5 illustrates that 6/16 two teeth SRM is able to provide comparable torque output with the PMSM. The high torque feature of this rare-earth free SRM demonstrates its potential for EV applications. Moreover, the total iron loss and motor theoretical calculated efficiency by utilizing FEM is shown in the following Fig. 6 and Fig. 7 under various speed condition.

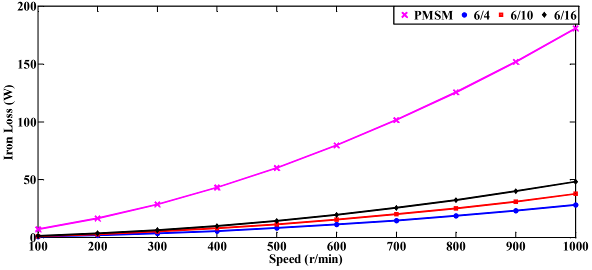

Fig. 6: Iron loss comparison under different speeds

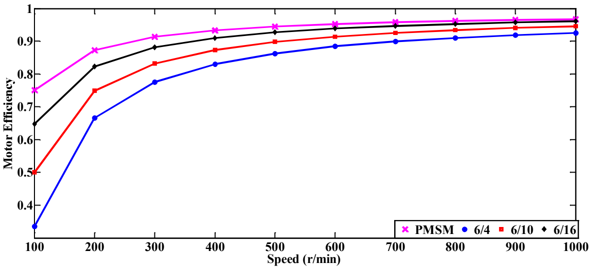

Fig. 7: Calculated motor efficiency comparison under various speeds condition

The comparison results in Fig. 6 show that the total iron loss of the PMSM is much higher than three SRMs due to the fact that the PMSM owns both core loss from the steel and eddy current loss from the PM material. 6/10 and 6/16 two-teeth SRM topology also increase total iron loss compared with the conventional counterpart because of smaller commutation angle and higher frequency of commutation. However, the iron loss of them is not as significant as that of the PMSM.

The efficiency comparison results shown in Fig. 7 demonstrate that the PMSM exhibits the highest efficiency for in-wheel applications. The existence of considerable copper loss due to more copper windings for SRMs decreases their efficiencies. The PMSM increases iron loss by utilizing PM material, but weakens its own copper loss more, thus leading to higher efficiency compared with other kinds of machines. 6/16 two-teeth SRM, however, also exhibits high efficiency for EV applications, which is quite similar to that of the PMSM at the rated speed. Additionally, 6/16 SRM topology does not contain any rare-earth materials. Therefore, it can be selected as an ideal candidate for the EV in-wheel motor. The performance comparison of the four topologies at the rated speed 1000 r/min can be found in the following Table II.

Table II
Performance Comparison of the Four Topologies

Dimensions	6/4 SRM	6/10 SRM	12/8 PMSM	6/16 SRM
Current density (A/mm^2)	5	5	5	5
RMS current (A)	39.4	39.4	39.4	39.4
Iron loss (W)	28	38	181	48
Copper loss (W)	576	1006	670	916
Torque (Nm)	91	209	284	271
Torque ripple (%)	85	58	32	48
Rated power (kW)	9.5	22	30	28
Coil end length (mm)	16	18	11	15
Torque density (Nm/L)	7.5	16.1	25.8	22.8
Efficiency (%)	92.6	94.6	96.7	96.2

From the above Table II, the torque density and efficiency of 6/16 SRM are quite similar to those of a PMSM. As a result, it can be considered as a competitive candidate for a high torque density rare-earth free in-wheel motor.

IV. CONCLUSION

In this paper, four topologies of in-wheel electric machines, including a surface-mounted PMSM and three SRMs, namely 6/4, 6/10 and 6/16 structures, are proposed for performance comparison. All the topologies are optimized for maximal torque output. The following analysis based on FEM demonstrates that 6/16 two-teeth SRM is able to provide comparable torque density with the PMSM of the same dimension, while conventional and 6/10 SRM exhibits much lower performance. Besides, the efficiency of it is quite similar to that of a PMSM. Therefore, it owns a vast potential for EV applications due to its rare-earth free feature.

REFERENCE

[1] Bin Zhang, Ronghai Qu, Jin Wang, Wei Xu, Xinggang Fan, and Yu Chen, “Thermal Model of Totally Enclosed Water-Cooled Permanent-Magnet Synchronous Machines for Electric Vehicle Application”, *IEEE Trans. Ind. Appl.*, vol. 51, no. 4, pp. 3020–3029, Jul./Aug. 2015.

[2] Apoorva Athavale, Kensuke Sasaki, Brent S. Gagas, Takashi Kato, and Robert D. Lorenz, “Variable Flux Permanent Magnet Synchronous Machine (VF-PMSM) Design Methodologies to Meet Electric Vehicle Traction Requirements with Reduced Losses”, *IEEE Trans. Ind. Appl.*, vol. 53, no. 5, pp. 4318–4326, Sep./Oct. 2017.

[3] Yue Zhang, Wenping Cao, Sean McLoone, and John Morrow, “Design and Flux-Weakening Control of an Interior Permanent Magnet Synchronous Motor for Electric Vehicles”, *IEEE Trans. Appl. Supercond.*, vol. 26, no. 7, Oct. 2016.

[4] Conggan Ma, Qing Li, Qinghe Liu, Dafang Wang, Jiajun Gao, Huiyao Tang, and Yanhua Sun, “Sound Quality Evaluation of Noise of Hub Permanent-Magnet Synchronous Motors for Electric Vehicles”, *IEEE Trans. Ind. Electron.*, vol. 63, no. 9, pp. 5663–5673, Sep. 2016.

[5] Ki-Chan Kim, “A Novel Calculation Method on the Current Information of Vector Inverter for Interior Permanent Magnet Synchronous Motor for Electric Vehicle”, *IEEE Trans. Magn.*, vol. 50, no. 2, Feb. 2014.

[6] Christopher H. T. Lee, James L. Kirtley, Jr., and M. Angle, “A Partitioned-Stator Flux-Switching Permanent-Magnet Machine With Mechanical Flux Adjusters for Hybrid Electric Vehicles”, *IEEE Trans. Magn.*, vol. 53, no. 11, Nov. 2017.

[7] Wei Hua, Gan Zhang, and Ming Cheng, “Investigation and Design of a High-Power Flux-Switching Permanent Magnet Machine for Hybrid Electric Vehicles”, *IEEE Trans. Magn.*, vol. 51, no. 3, Mar. 2015.

[8] Peng Su, Wei Hua, Gan Zhang, Zhe Chen, Ming Cheng, “Analysis and evaluation of novel rotor permanent magnet flux-switching machine for EV and HEV applications”, *IET Electr. Power Appl*, vol. 11, no. 9, pp. 1610-1618, 2017.

[9] Ju Hyung Kim, Yingjie Li, and Bulent Sarlioglu, “Novel Six-Slot Four-Pole Axial Flux-Switching Permanent Magnet Machine for Electric Vehicle”, *IEEE Trans. Transport. Electrific.*, vol. 3, no. 1, pp. 108–117, Mar. 2017.

[10] Saurabh P. Nikam, Vandana Rallabandi, and B. G. Fernandes, “A High-Torque-Density Permanent-Magnet Free Motor for in-Wheel Electric Vehicle Application”, *IEEE Trans. Ind. Appl.*, vol. 48, no. 6, pp. 2287–2295, Nov./Dec. 2012.

[11] Vandana Rallabandi, Baylon Godfrey Fernandes, “Design procedure of segmented rotor switched reluctance motor for direct drive applications”, *IET Electr. Power Appl*, vol. 8, no. 3, pp. 77-88, 2014.

[12] Khwaja M. Rahman and Steven E. Schulz, “Design of High-Efficiency and High-Torque-Density Switched Reluctance Motor for Vehicle Propulsion”, *IEEE Trans. Ind. Appl.*, vol. 38, no. 6, pp. 1500–1507, Nov./Dec. 2002.

[13] Akira Chiba, Kyohei Kiyota, Nobukazu Hoshi, Masatsugu Takemoto, and Satoshi Ogasawara, “Development of a Rare-Earth-Free SR Motor With High Torque Density for Hybrid Vehicles”, *IEEE Trans. Energy Convers.*, vol. 30, no. 1, pp. 175–182, Mar. 2015.

[14] Z. Q. Zhu and J. T. Chen, “Advanced Flux-Switching Permanent Magnet Brushless Machines”, *IEEE Trans. Magn.*, vol. 46, no. 6, pp. 1447-1453, Jun. 2010.

[15] Berker Bilgin, Ali Emadi and Mahesh Krishnamurthy, “Design Considerations for Switched Reluctance Machines With a Higher Number of Rotor Poles”, *IEEE Trans. Ind. Electron.*, vol. 59, no. 10, pp. 3745–3756, Oct. 2012.

[16] Jingwei Zhu, Ka Wai Eric Cheng, Xiangdang Xue, Yu Zou, “Design of a New Enhanced Torque In-Wheel Switched Reluctance Motor with Divided Teeth for Electric Vehicles”, *IEEE Trans. Magn.,* vol. 53, no. 11, Nov. 2017.

[17] X. D. Xue, K.W.E. Cheng, T.W. Ng, and N. C. Cheung, “Multi-Objective Optimization Design of In-Wheel Switched Reluctance Motors in Electric Vehicles”, *IEEE Trans. Ind. Electron.*, Vol. 57, No. 9, pp. 2980 – 2987, Sep. 2010.

Asian Power Electronics Journal, Vol. 12, No. 1, June 2018

Loss Analysis of Hybrid Battery-Supercapacitor Energy Storage System in EVs

Xue X. D.   Raghu Raman S   Fong Y. C.   Cheng K. W. E.

Abstract–In this study, the losses of the hybrid energy storage system (HESS) including super-capacitor (SC) and battery in an electric vehicle (EV) are analyzed. Based on the presented vehicular system structure, the simulation model is proposed. With the controllable super-capacitor current, the operation of an EV with the hybrid battery-supercapacitor energy storage system is simulated under the European urban driving schedule ECE-15 and the losses of the hybrid energy system are computed and analyzed. The simulated results demonstrate that the super-capacitor current can be optimized under various operating conditions to minimize the losses of the hybrid battery-supercapacitor energy storage system in the EV. Thus, this study provides the valuable approach to maximize the operating efficiency of the hybrid battery-supercapacitor energy storage system in EVs.

Keywords–Battery, efficiency, electric vehicles (EV), hybrid energy storage system (HESS), losses, super-capacitor.

I. INTRODUCTION

Energy storage system is one of the important components in electric vehicles. In general, such an energy storage system consists of an energy storage component, two or more than two components. The latter is named as the hybrid energy storage system, such as the hybrid battery-supercapacitor energy storage system. As known well, battery has high specific energy and low specific power. However, super-capacitor has high specific power and low specific energy. Obviously, dynamic performance of super-capacitor energy storage system is better than battery energy storage system. Consequently, the hybrid battery-supercapacitor energy storage system can improve dynamic performance of battery energy storage system. Therefore, dynamic performance of the EV with hybrid battery-supercapacitor energy storage system can be better than the EV with battery energy storage system. In addition, the super-capacitor has the advantage of fast charge and the hybrid battery-supercapacitor energy storage system can extend battery life time.

For the constant car velocity, the study in [1] shows that the optimal ratio of the super-capacitor power to the bus power can be found to minimize the losses of the hybrid battery-supercapacitor energy storage system. An optimization algorithm is proposed to extend battery life time and simultaneously to improve the energy efficiency of the hybrid battery-supercapacitor energy storage system [2]. A power optimization method is proposed in [3] to have the minimum battery loss. In [4], the topologies of the converters for connecting super-capacitor to battery are analyzed and the current control method for bidirectional non-isolated converters is presented to realize the power flow arrangement. The reference [5] deals with a multi-objective optimization problem for optimizing the power split to extend the battery lifetime and to reduce the power losses of the hybrid battery-supercapacitor energy storage system, and the online energy management controller is proposed. Different converter topologies for the hybrid battery-supercapacitor energy storage system are discussed in [6].

This paper focuses on the loss analysis of the hybrid battery-supercapacitor energy storage system in EVs. In the remaining sections of this paper, the schematic system structure of the EV with hybrid battery-supercapacitor energy storage system will be presented. Then, the dynamic model of such a system structure will be proposed. Next, an EV prototype with the hybrid battery-supercapacitor energy storage system will be simulated under the European urban driving schedule ECE-15. After that, the losses of the battery and the super-capacitor will be studied and analyzed. Finally, the conclusion will be shown.

II. MODEL OF EV SYSTEM

1. System Structure of EV with Hybrid Battery-Supercapacitor Energy Storage System

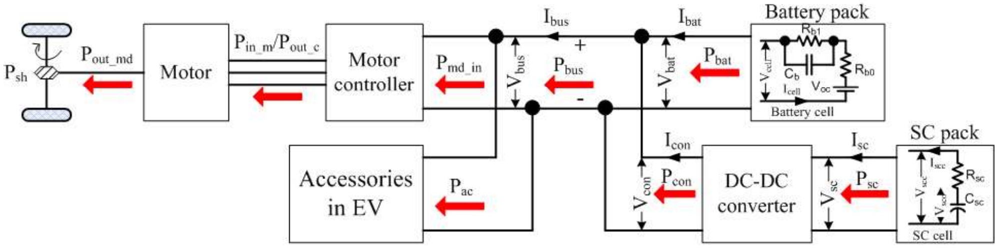

Fig. 1: Schematic structure of EV system with hybrid battery-supercapacitor energy storage system

The schematic system structure of the EV with hybrid battery-supercapacitor energy storage system is illustrated in Fig. 1, where C_{sc} represents the capacitance of the SC

Department of Electrical Engineering, The Hong Kong Polytechnic University, Hong Kong, China
E-mail: xd.xue@polyu.edu.hk, raghu.s.raman88@gmail.com, 14900129r@connect.polyu.hk, eeecheng@polyu.edu.hk

cell, R_{sc} the internal resistance of the SC cell, I_{scc} the current of the SC cell, V_{sco} the open-circuit voltage of the SC cell, V_{scc} the voltage across the SC cell, I_{sc} the current of the SC pack, V_{sc} the voltage of the SC pack, V_{con} the voltage of the dc-dc converter, I_{con} the current of the dc-dc converter, C_b the equivalent capacitance of the battery cell, R_{b0} and R_{b1} the equivalent internal resistances of the battery cell, I_{cell} the current of the battery cell, V_{oc} the open-circuit voltage of the battery cell, V_{cell} the voltage across the battery cell, I_{bat} the current of the battery pack, V_{bat} the voltage of the battery pack, V_{bus} the bus voltage, I_{bus} the bus current, P_{sc} the power of the SC pack, P_{bat} the power of the battery pack, P_{bus} the bus power, P_{in_md} the input power of the motor drive including the motor and the motor controller, P_{out_c} the output power of the motor controller, P_{in_m} the input power of the motor, P_{out_c} is equal to P_{in_m}, P_{out_md} the output power of the motor drive, the P_{sh} the shaft power of the EV, and P_{ac} the average power of the accessories in the EV.

2. Model of EV System

Referring to Fig. 1, the discharging current of the SC cell is computed as

$$I_{scc} = \frac{V_{sco} - \sqrt{V_{sco}^2 - 4R_{sc}P_{scc}}}{2R_{sc}} \tag{1}$$

where P_{scc} is the power of the SC cell.

The charging current of the SC cell is expressed as

$$I_{scc} = -\frac{-V_{sco} + \sqrt{V_{sco}^2 - 4R_{sc}P_{scc}}}{2R_{sc}} \tag{2}$$

Moreover, I_{scc} can be computed as

$$I_{scc} = C_{sc}\frac{dV_{sco}}{dt} \tag{3}$$

The depth of discharge for the SC pack is computed as

$$DoD_{sc} = \frac{V_{scmax}^2 - V_{sc}^2}{V_{scmax}^2 - V_{scmin}^2} \tag{4}$$

where V_{scmax} represents the maximum operating voltage of the SC pack, and V_{scmin} the minimum operating voltage of the SC pack.

For the battery, the discharging current of the battery cell is computed as

$$I_{cell} = \frac{V_{oc} - \sqrt{V_{oc}^2 - 4(R_{b0} + R_{b1})P_{cell}}}{2(R_{b0} + R_{b1})} \tag{5}$$

where P_{cell} represents the power of the battery cell.

The open-circuit voltage of the battery cell can be estimated as

$$V_{oc} = \sum_{j=0}^{19} c_j\,(SoC - SoC_{ave})^j \tag{6}$$

where SoC is the state of charge of the battery, c_j and SoC_{ave} are the constant values for the given lithium battery, respectively.

The battery SoC is can be expressed as

$$SoC = \frac{C_r}{C_n} \tag{7}$$

where C_r is the remaining charge and C_n the nominal charge.

The power of the dc-dc converter is computed as

$$P_{con} = I_{con}V_{con} \tag{8}$$

If the SC pack runs under discharging, the relationship between the input and the output of the dc-dc converter can be expressed as

$$P_{con} = \eta_{con}P_{sc} \tag{9}$$

If the SC pack runs under charging,, the relationship between the input and the output of the dc-dc converter can be expressed as

$$\eta_{con}P_{con} = P_{sc} \tag{10}$$

where η_{con} represents the efficiency of the dc-dc converter.

The power of the battery pack is expressed as

$$P_{bat} = I_{bat}V_{bat} \tag{11}$$

The bus power is calculated as

$$P_{bus} = P_{in\_md} + P_{ac} \tag{12}$$

and

$$P_{bus} = P_{bat} + P_{con} \tag{13}$$

The efficiency of the motor drive can be estimated as [7]

$$\eta_{md} = \frac{T_m\omega_m}{T_m\omega_m + k_{cu}T_m^2 + k_{fe}\omega_m + k_w\omega_m^3 + p_{lmd}} \tag{14}$$

where T_m is the motor torque, ω_m is the angular speed of the motor, k_{cu} is the coefficient of copper loss, k_{fe} the coefficient of iron loss, k_w the coefficient of windage loss, p_{lmd} the constant loss arising from the motor controller and the motor.

Under driving/motoring operation, one has

$$\eta_{md}P_{in\_md} = P_{out\_md} \tag{15}$$

$$\eta_g P_{out\_md} = P_{sh} \tag{16}$$

Under braking/generating operation, otherwise, one has

$$P_{out\_md} = \eta_g P_{sh} \tag{17}$$

$$P_{in\_md} = \eta_{md}P_{out\_md} \tag{18}$$

where η_g represents the efficiency of the gear device and can be regarded as a constant.

The shaft power can be expressed as

$$P_{sh} = \frac{G_r}{r_t} T_m v \tag{19}$$

where v is the velocity of the EV, G_r the gear ratio of the gear device connecting the motor to the shaft and is a constant, and r_t the radius of the tire.

The electromechanical dynamic equation of an EV can be expressed as

$$m\frac{dv}{dt} = \frac{G_r}{r_t} T_m - \mu_{rr} mg - \frac{1}{2}\rho A C_d v^2 - mg sin\theta \tag{20}$$

where m is the total mass of the EV, t the time, μ_{rr} the coefficient of rolling resistance and can be regarded as a constant, g the gravitational acceleration, ρ the density of the air and can be regarded as a constant, A the front area of the EV, C_d the drag coefficient and can be regarded as a constant, and θ the angle between the slope and the level ground.

The losses of the battery pack and the SC pack are calculated as, respectively,

$$P_{loss\_bat} = I_{bat}^2 r_{batp} \tag{21}$$

$$P_{loss\_sc} = I_{sc}^2 r_{scp} \tag{22}$$

where r_{batp} is the equivalent resistance of the battery pack and r_{scp} is the equivalent resistance of the SC pack.

In a driving cycle, the average battery loss and the average SC loss are computed as, respectively,

$$P_{loss\_bat\_c} = \sum(P_{loss\_bat}\Delta t)/T_c \tag{23}$$

$$P_{loss\_sc\_c} = \sum(P_{loss\_sc}\Delta t)/T_c \tag{24}$$

where Δt is the sampling time and T_c is the time of a driving cycle.

In a full discharging cycle, thus, the average battery loss and the average SC loss are computed as, respectively,

$$P_{loss\_bat\_r} = \sum(P_{loss\_bat\_c}T_c)/T_r \tag{25}$$

$$P_{loss\_bat\_r} = \sum(P_{loss\_sc\_c}T_c)/T_r \tag{26}$$

where T_r is the time of a full discharging cycle.

III. SIMULATION OF EV OPERATION UNDER EUROPEAN URBAN DRIVING SCHEDULE ECE-15

1. Main Data of EV Prototype

The main data of an EV prototype is shown in Table 1. Such an EV prototype is simulated to study the effects of both the SC current and the SC capacity on the losses of the hybrid battery-supercapacitor energy storage system.

2. European Urban Driving Schedule ECE-15

The European urban driving schedule ECE-15 is suitable for examining the performance of the EV prototype in this paper. Fig. 2 shows a driving cycle of the European urban driving schedule ECE-15.

3. Strategy of Energy Management

In this study, the strategy of the energy management is proposed as follows. (a) If the bus power is less than 0, the SC is only charged; (b) under the condition that the SC voltage is more than the minimum SC voltage and the battery DoD is less than 0.8, if the bus power is more than 0, both the SC and the battery discharge; (c) under the condition that the SC voltage is less than or equal to the minimum SC voltage and the battery DoD is less than 0.8, if the bus power is more than 0, the battery discharges; (d) under the condition that the SC voltage is more than the minimum SC voltage and the battery DoD is more than or equal to 0.8, if the bus power is more than 0, the SC discharges; and (e) if the SC voltage is less than or equal to the minimum SC voltage and the battery DoD is more than or equal to 0.8, both the SC and the battery do not operate and the simulation ends.

Table 1: Main data of EV prototype

Parameters	Value
Model of prototype	Two-door and two-seat light EV
Total mass	790 kg
Radius of tyre	0.275 m
Gear ratio	8.25
Rated velocity	50 km/m
Maximum velocity	70 km/m
Rated power of motor	5 kW
HESS	Lithium battery and super-capacitor

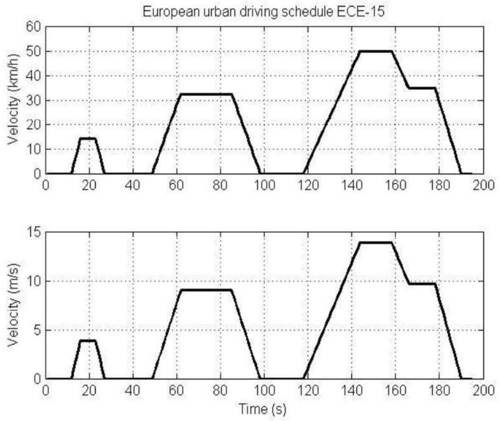

Fig. 2: Driving cycle of European urban driving schedule

4. Simulated Results

If the battery capacity is 4477.0 Wh, the SC capacity is 1877.778 Wh and the ratio of the SC current to the battery is 0.5, the operating performances of the EV are simulated and shown in Fig. 3. Figs. 3a-3c illustrate the operating performances during a full discharging period and Figs. 3d-3i show the operating performances during the 40th driving cycle.

It can be seen from Figs. 3 that the simulated results indicate the real operation of the EV. Furthermore, it is easy that the simulated results are verified by the theoretical analysis.

IV. EFFECTS OF SC CURRENT AND SC CAPACITY ON BATTERY AND SC LOSSES UNDER EUROPEAN URBAN DRIVING SCHEDULE ECE-15

1. Case A

In the case A, the capacity of the battery is 4477.0 Wh and the capacity of the SC is 1877.778 Wh. Thus, the ratio of the SC capacity to the battery capacity is 0.419428. The effects of the SC current on the battery loss, the SC loss and the sum of both are illustrated in Fig. 4. It can be seen from Fig. 4 that (a) there is the optimal SC current and the optimal ratio of the SC current to the battery current is 0.5, to obtain the minimum average battery loss during a full discharging period, (b) there is the optimal SC current and the optimal ratio of the SC current to the battery current is 0.6, to obtain the minimum average SC loss during a full discharging period, and (c) there is the optimal SC current and the optimal ratio of the SC current to the battery current is 0.5, to obtain the minimum sum of the average battery loss and the average SC loss during a full discharging period.

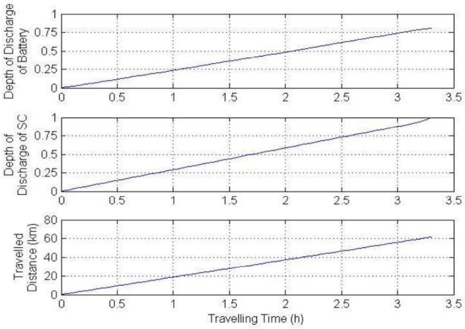

(a) Battery DoD, SC DoD and travelled distance during a full discharging period

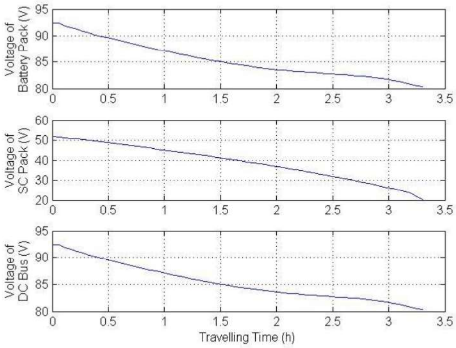

(b) Battery voltage, SC voltage, DC bus voltage during a full discharging period

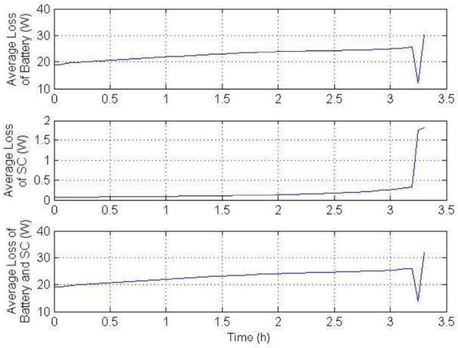

(c) Average battery loss, average SC loss and sum of both during a full discharging period

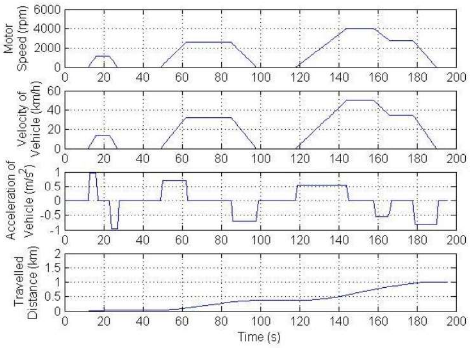

(d) Motor speed, car velocity, car acceleration and travelled distance during 40th driving cycle

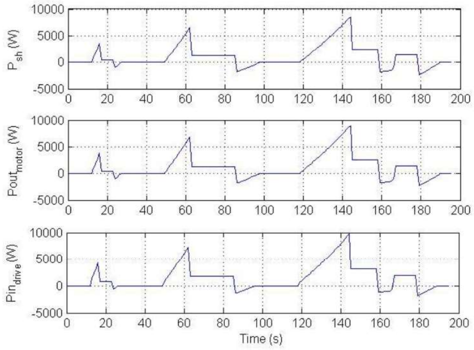

(e) Shaft power, motor output power and input power of motor drive during 40th driving cycle

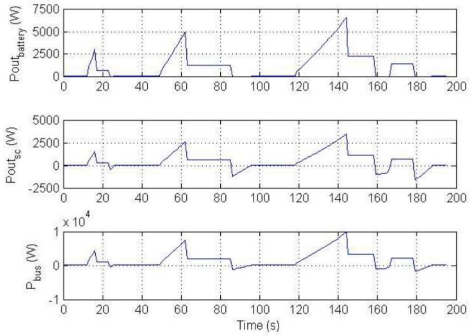

(f) Battery power, SC power and bus power during 40th driving cycle

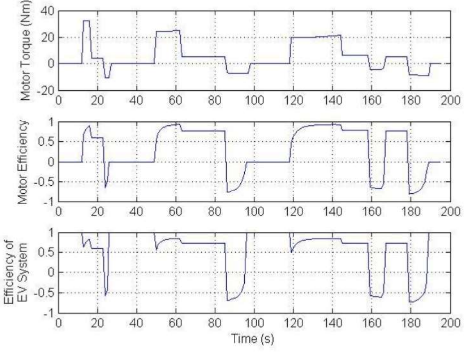

(g) Motor torque, efficiency of motor drive and efficiency of EV system during 40th driving cycle

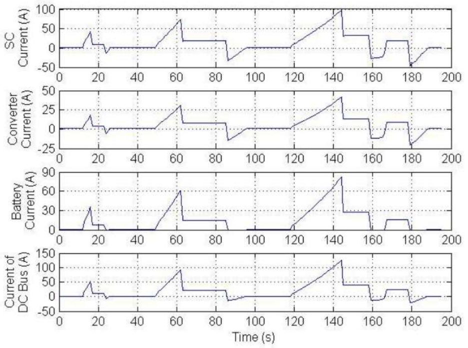

(h) SC current, converter current, battery current, and bus current during 40th driving cycle

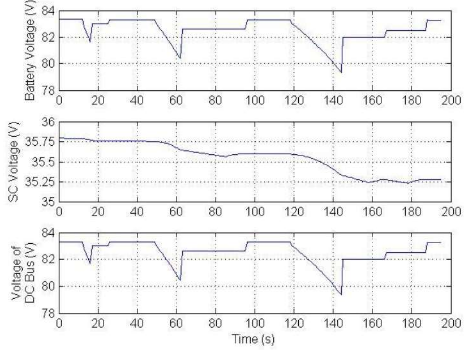

(i) Battery voltage, SC voltage, and bus voltage during 40th driving cycle

Fig. 3: Simulated waveforms under European urban driving schedule ECE-15

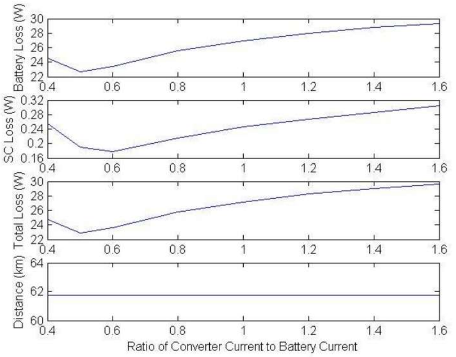

Fig. 4 Effect of SC current on losses (Battery capacity = 4477.000 Wh and SC capacity = 1877.778 Wh)

2. Case B

In this case, the capacity of the battery is 4477.0 Wh and the capacity of the SC is 3755.556 Wh. Thus, the ratio of the SC capacity to the battery capacity is 0.838855. The effects of the SC current on the battery loss, the SC loss and the sum of both are illustrated in Fig. 5. It can be seen from Fig. 5 that (a) there is the optimal SC current and the optimal ratio of the SC current to the battery current is 1.0, to obtain the minimum average battery loss during a full discharging period, (b) there is the optimal SC current and the optimal ratio of the SC current to the battery current is 1.0, to obtain the minimum average SC loss during a full discharging period, and (c) there is the optimal SC current and the optimal ratio of the SC current to the battery current is 1.0, to obtain the minimum sum of the average battery loss and the average SC loss during a full discharging period.

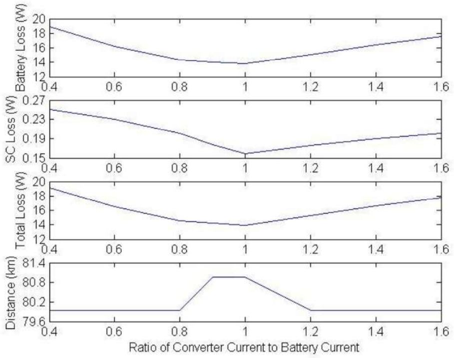

Fig. 5: Effect of SC current on losses (Battery capacity = 4477.000 Wh and SC capacity = 3755.556 Wh)

3. Case C

In the case C, the capacity of the battery is 4477.0 Wh and the capacity of the SC is 5633.333 Wh. Thus, the ratio of the SC capacity to the battery capacity is 1.258283. The effects of the SC current on the battery loss, the SC loss and the sum of both are illustrated in Fig. 6. It can be seen from Fig. 6 that (a) there is the optimal SC current and the optimal ratio of the SC current to the battery current is 1.4, to obtain the minimum average battery loss during a full discharging period, (b) there is the optimal SC current and the optimal ratio of the SC current to the battery current is 1.4, to obtain the minimum average SC loss during a full discharging period, and (c) there is the optimal SC current and the optimal ratio of the SC current to the battery current is 1.4, to obtain the minimum sum of the average battery loss and the average SC loss during a full discharging period.

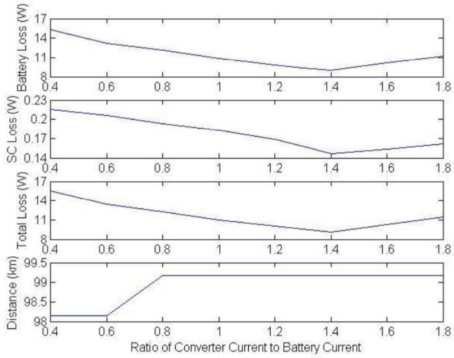

Fig. 6: Effect of SC current on losses (Battery capacity = 4477.000 Wh and SC capacity = 5633.333 Wh)

4. Relationship between Optimal SC Current and Capacities

From the aforementioned simulated results and analysis, it can be seen that the SC current can be optimized for the minimum battery loss, the minimum SC loss or the minimum sum of both, and that the optimal SC current depends on the ratio of the SC capacity to the battery capacity. The effect of the ratio of the SC capacity to the battery capacity on the optimal ratio of the SC current to the battery is illustrated in Fig. 7. It can be observed from Fig. 7 that the optimal ratio of the SC current to the battery current changes with the ratio of the SC capacity to the battery capacity.

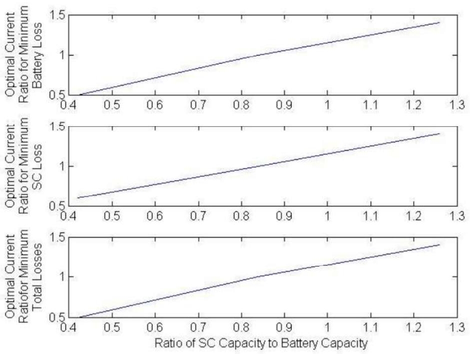

Fig. 7: Effect of ratio of SC capacity to battery capacity on optimal ratio of SC current to battery current

V. CONCLUSION

The dynamic model of the EV with the hybrid battery-supercapacitor energy storage system is proposed. Based on the proposed dynamic model, an EV prototype has been simulated under the European urban driving schedule and the proposed energy management strategy. The study shows that (a) for an EV with a hybrid battery-supercapacitor energy storage system the super-capacitor current can be optimized to have the minimum battery loss, the minimum super-capacitor loss, or the minimum sum of the battery loss and the super-capacitor loss, (b) the optimal super-capacitor current depends on both the battery capacity and the super-capacitor capacity, and (c) the optimal ratio of the super-capacitor current to the battery current increases with increase in the ratio of the super-capacitor capacity to the battery capacity. Thus, this paper offers the valuable investigation for the maximum efficiency control of the hybrid battery-supercapacitor energy storage system in EVs.

ACKNOWLEDGMENT

The authors would like to thank the part financial support from the Innovation and Technology Fund of Hong Kong Innovation and Technology Support Programme under Grant GHP/057/14AP.

REFERENCES

[1] X. D. Xue, K. W. E. Cheng, Raghu Raman S, Y. C. Fong, and X. L. Wang, “Investigation of Energy Distribution and Power Split of Hybrid Energy Storage Systems in Electric Vehicles”, *2016 International Symposium on Electrical Engineering* (ISEE), 2016, Hong Kong, China, pp.1-7.

[2] He Yin, Chen Zhao, Mian Li, and Chengbin Ma, “Optimization Based Energy Control for Battery/Super-capacitor Hybrid Energy Storage Systems”, *IECON 2013* 2013, pp. 6764-6769.

[3] Tongjing Wang, Weiwen Deng, Jian Wu and Qiao Zhang, “Power Optimization for Hybrid Energy Storage System of Electric Vehicle”, *ITEC Asia-Pacific 2014*, pp. 1-6.

[4] Huang Xiaoliang, Hori Yoichi, and Hiramatsu Tosiyoki, “Bidirectional Power Flow Control for Battery Super Capacitor Hybrid Energy System for Electric Vehicles with In-Wheel Motors”, *16th International Power Electronics and Motion Control Conference and Exposition*, Antalya, Turkey 21-24 Sept 2014, pp. 1078-1083.

[5] Junyi Shen and Alireza Khaligh, “A Supervisory Energy Management Control Strategy in a Battery/Ultracapacitor Hybrid Energy Storage System”, *IEEE Transactions on Transportation Electrification*, VOL. 1, NO. 3, OCTOBER 2015, pp. 223-231.

[6] S. Raghu Raman, Y.C. Fong, X.D. Xue, K.W.E. Cheng, “Hybrid Energy Storage System for Electric Vehicles with Body Integrated Super Capacitors”, presented at 2017 International Conference on Power Electronics Systems and Applications (PESA 2017), Hong Kong, China, Dec 2017

[7] Lowry, John, and Larminie, James, *Electric Vehicle Technology Explained* (2nd Edition). Somerset, NJ, USA, John Wiley & Sons, 2012.

Author Index

Submission Details

Only online submission will be accepted. Please first register and submit online. The paper is in double column and is similar to most IET or IEEE journal format. There is no page limit. Any number of pages of more than 6 will be subject to additional charge.

The paper guidelines can be downloaded using the link: http://perc.polyu.edu.hk/apejournal/

Any queries, please contact Prof. Eric Cheng, Publishing Director of APEJ, Dept. of Electrical Engineering, The Hong Kong Polytechnic University, Hung Hom, Hong Kong. Email: eeecheng@polyu.edu.hk Fax: +852-2330 1544

Any secretarial support and production related matters, please contact Dr. James Ho, Power Electronics Research Centre, The Hong Kong Polytechnic University, Hung Hom, Hong Kong. Email: eeapej@polyu.edu.hk Tel: +852-3400 3348 Fax: +852-3400 3343

Publication Details

The Journal will be published 2-3 times a year. The first issue was published in 2007. Response time for paper acceptance is within 3 months.

Financial Charge

All the accepted papers will be printed without charge for 6 or less pages. An additional page charge is HK$100 per page. A hardcopy of the journal will be posted to the corresponding author free of charge. Additional copies of the journal can be purchased at HK$200 each. The charge includes postage and packing.

All Chinese Papers will be subjected to a translational fee of HK$350 per page. It will be charged when the paper is accepted for publication.

Advertising

Advertisement is welcome. Full page advertisement is HK$1000. For colour advertisement, the amount is doubled. All the advertisement will be both posted online in the journal website and hardcopy of the journal.

For advertising enquiries and details, please contact Ms. Anna Chang, eeapej@polyu.edu.hk .
Tel: +852-3400 3348 Fax: +852-3400 3343

For payment, please send your cheque, payable to ‘The Hong Kong Polytechnic University, address to Ms. Kit Chan, Secretary of APEJ, Dept. of Electrical Engineering, The Hong Kong Polytechnic University, Hung Hom, Hong Kong.